A&A 633, A10 (2020)
https://doi.org/10.1051/0004-6361/201936463

Astronomy & Astrophysics

Influence of sub- and super-solar metallicities on the composition of solid planetary building blocks

Bertram Bitsch[1] and Chiara Battistini[2]

[1] Max-Planck-Institut für Astronomie, Königstuhl 17, 69117 Heidelberg, Germany
e-mail: bitsch@mpia-hd.mpg.de
[2] Zentrum für Astronomie der Universität Heidelberg, Landessternwarte Königstuhl, Königstuhl 12, 69117 Heidelberg, Germany

Received 5 August 2019 / Accepted 21 November 2019

ABSTRACT

The composition of the protoplanetary disc is thought to be linked to the composition of the host star, where a higher overall metallicity provides the building blocks for planets. However, most of the planet formation simulations only link the stellar iron abundance [Fe/H] to planet formation and the iron abundance in itself is used as a proxy to scale all elements. On the other hand, large surveys of stellar abundances show that this is not true. Here we use stellar abundances from the GALAH surveys to determine the average detailed abundances of Fe, Si, Mg, O, and C for a broad range of host star metallicities with [Fe/H] spanning from −0.4 to +0.4. Using an equilibrium chemical model that features the most important rock-forming compounds as well as volatile contributions of H_2O, CO_2, CH_4, and CO, we calculate the chemical composition of solid planetary building blocks around stars with different metallicities. Solid building blocks that are formed entirely interior to the water ice line ($T > 150$ K) only show an increase in Mg_2SiO_4 and a decrease in $MgSiO_3$ for increasing host star metallicity, which is related to the increase of [Mg/Si] for higher [Fe/H]. Solid planetary building blocks forming exterior to the water ice line ($T < 150$ K), on the other hand, show dramatic changes in their composition. In particular, the water ice content decreases from around ∼50% at [Fe/H] = −0.4 to ∼6% at [Fe/H] = 0.4 in our chemical model. This is mainly caused by the increasing C/O ratio with increasing [Fe/H], which binds most of the oxygen in gaseous CO and CO_2, resulting in a small water ice fraction. Planet formation simulations coupled with the chemical model confirm these results by showing that the water ice content of super-Earths decreases with increasing host star metallicity due to the increased C/O ratio. This decrease of the water ice fraction has important consequences for planet formation, planetary composition, and the eventual habitability of planetary systems formed around these high-metallicity stars.

Key words. planets and satellites: composition – planets and satellites: formation – stars: abundances

1. Introduction

Observations of exoplanets have revealed that close-in super-Earths are the most abundant type of planet within 1 AU (Mayor et al. 2011; Mulders et al. 2018; Zhu & Wu 2018). These super-Earths typically have masses of a few Earth masses; planets within the same system could be of similar size (Weiss et al. 2018) and, thus, presumably of a similar mass, although recent analyses have questioned this correlation (Zhu 2019).

These super-Earths exist around many different type of stars, even around small M-dwarfs (Gillon et al. 2016, 2017). Moreover, there seems to be no trend for host star metallicity with regard to the occurrence rate of these super-Earths (Buchhave et al. 2012). This seems to make super-Earths the most robust outcome of planet formation in nature.

However, Sousa et al. (2019) found that planets below 30 Earth masses seem to have a positive correlation with the host star metallicity-period-mass diagram, meaning that the mass of the planet increases with both host star metallicity and orbital period. The trend of planetary masses increasing with host star metallicity is not surprising as giant planets are more common around host stars with a higher metallicity (Santos et al. 2004; Fischer & Valenti 2005; Johnson et al. 2010). The trend with orbital distance could also be explained by the host star metallicity. If more building blocks are available, planetary embryos at larger distances can also grow faster and form planets through the accretion of pebbles (Bitsch et al. 2015b), which could explain these trends and could also give rise to the giant planet eccentricity distribution (Buchhave et al. 2018).

If the planetary radius through transit observations and the planetary masses through RV detections are known, the mean density of the planet can be calculated (e.g. see Dorn et al. 2018 for the Trappist-1 system). This can provide important information about the planetary composition through interior structure models (Valencia et al. 2007; Sotin et al. 2007; Seager et al. 2007; Fortney et al. 2007; Selsis et al. 2007; Adams et al. 2008; Zeng & Sasselov 2013; Buchhave et al. 2016) which, in turn, can provide important information about the formation history of the planet and its evolution (Vazan et al. 2018). Planets with mean densities close to the terrestrial planets were most likely formed in the inner regions of the protoplanetary disc without any significant accretion of water ice, while planets with lower densities could harbour a significant fraction of water ice (Zeng et al. 2019). Of course, the planetary radius measurements could be greatly influenced by planetary atmospheres.

The formation pathways of these super-Earths, on the other hand, is still under debate and a lot of different theories have been proposed (Terquem & Papaloizou 2007; Ida & Lin 2008, 2010; Ogihara & Ida 2009; McNeil & Nelson 2010; Hansen & Murray 2012; Cossou et al. 2014; Chatterjee & Tan 2014; Ogihara et al. 2015; Lee & Chiang 2016; Izidoro et al. 2017). Studies that consider super-Earths forming in the outer parts of the disc

and then letting them migrate into the inner regions have the advantage that they can naturally explain water-rich super-Earths (Raymond et al. 2018; Izidoro et al. 2019; Bitsch et al. 2019b; Schoonenberg et al. 2019). However, the formation pathway of forming super-Earths in the outer disc and then migrating them inwards depends crucially on the water fraction within the protoplanetary disc because it influences the growth and migration pathway of planets (Bitsch & Johansen 2016).

Planet formation simulations that include chemical models have mostly used a solar-like composition. These models either operate in the classical planetesimal accretion scenario (Bond et al. 2010; Marboeuf et al. 2014; Thiabaud et al. 2015; Ronco et al. 2015), in the scenario of planet formation assisted at planet migration traps (Alessi et al. 2017; Cridland et al. 2019), or they include pebble accretion (Ali-Dib 2017; Madhusudhan et al. 2017). Some of these models additionally focus on the chemical abundances of the planetary atmospheres (Ali-Dib 2017; Madhusudhan et al. 2017; Cridland et al. 2019), while others mainly focus on the chemical composition of rocky or icy super-Earths (Alessi et al. 2017). Here we want to focus on the chemical composition of solid planetary building blocks which is set by the underlying chemical composition of the disc, rather than focus on the underlying physics necessary for planet formation theories.

The process of planet formation is thought to happen within the protoplanetary disc surrounding the newly formed star. A key assumption in models of planet formation is that the elemental abundances of the protoplanetary disc are directly correlated to the host star, meaning that the disc and the host star have the same elemental composition. However, in planet formation simulations, it is not very often taken into account that stellar elemental abundances show different trends when compared to [Fe/H]. In addition, most studies of planet formation have only focused on solar-like composition for the different elements.

These different elemental trends in stars are caused by the fact that different elements are produced in different kind of stars at different times in the galactic evolution (Burbidge et al. 1957). Elements like O, Mg, Si, Ca, Ti (also known as α-elements), as well as S, are mostly produced in massive stars during their evolution and then released in the interstellar space during supernovae explosions (Type II supernovae, SNII): this means that this enrichment is expected to happen on a short timescale (Matteucci & Greggio 1986). Low mass stars instead can pollute the interstellar medium on a longer time scale via, for example, Type Ia supernovae (SNIa), where significant quantities of Fe are released and only small fraction of α-elements (e.g. Thielemann et al. 2002). SNIa are created from white dwarfs in binary systems, resulting in a time delay relative to SNII (e.g. Matteucci et al. 2009) in a range between 0.3 and 1 Gyr (e.g. Valiante et al. 2009). It is important to know that even if different elements share the same production site (like SNII), the difference in mass of the progenitor star and/or the explosion parameters matters (Kobayashi et al. 2006; Kobayashi & Nakasato 2011) for the elemental yields and thus how they are incorporated to molecular clouds that form new stars.

Several works showed the trend of α-elements in respect to [Fe/H] in different sample sizes and different parts of the Galaxy (e.g. Adibekyan et al. 2012; Smiljanic et al. 2014; Bensby et al. 2014, 2017; Buder et al. 2018). Elements in different elemental groups (light elements, iron-peak elements, and neutron-capture elements) might have different trends simply because they are formed in different sites (see for example Bensby et al. 2014; Battistini & Bensby 2015, 2016). However, these trends have only been taken into account in a very small sample of studies related to planet formation and composition.

Recent studies have also focused on the mineralogy of super-Earth planets and how it could vary with stellar abundance (Unterborn & Panero 2017; Hinkel & Unterborn 2018; Putirka & Rarick 2019) or how the planet's formation very close to its host stars, where the temperatures are very high, changes the compounds that form the planet (Dorn et al. 2019). These studies took only the formation interior to the water ice line ($T > 150$ K) into account. Putirka & Rarick (2019) focus on the mantle mineralogy. Ligi et al. (2019) link detailed stellar observations of HD 219134 to constrain the properties of its planetary companions and determine the core to mantle ratio of these planets. The work by Santos et al. (2017) follows a different approach by studying the chemical composition of planetary building blocks around thin and thick disc stars in general, showing that the planetary building blocks differ in their iron and water mass fraction. Cabral et al. (2019) use stellar population synthesis simulations to predict the chemical composition of planetary building blocks using the same chemical model as Santos et al. (2017), finding similar results.

Here we combine detailed stellar abundance measurements of C, O, Mg, Si and S[1], from the GALAH survey to calculate the bulk composition of solid planetary building blocks. We do not distinguish in this study planetary host stars and stars that have no detected planets because the formation of planets seems to be an universal process, where nearly all stars should generally be expected to host planets within 1 AU (Mulders et al. 2018). For simplification, we mainly focus on the individual solid planetary building blocks, rather than incorporating them in a complex planet formation model (see Appendix C). Thus, we focus on solids that either form completely interior or exterior to the water ice line.

Our paper is structured as follows. In Sect. 2, we describe our chemical model and the calculation of the solid planetary building blocks. In Sect. 3, we show the compositions of solids formed around host stars with different metallicities and for solids formed completely interior and exterior to the water ice line. In Sect. 4, we apply the chemical model used to calculate the solid planetary building blocks to a planet formation model and show the final water ice content of the formed planets. We then discuss the implications of our results in Sect. 5 and summarize our findings in Sect. 6.

2. Methods

2.1. Stellar abundances

For our study, we used stellar abundances derived for the second data release of the GALAH (Galactic Archeology with HERMES) survey (Buder et al. 2018) that contains 342 682 stars. GALAH is a high-resolution ($R \sim 28\,000$), large-scale stellar spectroscopic survey of Milky Way stars in the magnitude range $12 < V < 14$ probing mostly the Galactic thin and thick disc but also a consistent number of halo stars. The Hermes spectrograph allows for observations in four discrete optical wavelength bands (4713–4903 Å, 5648–5873 Å, 6478–6737 Å and 7585–7887 Å) which means that for our studies, sulfur is not included in the

[1] S is not directly measured in the GALAH survey, but we assume it scales with [Fe/H] the same as Si, as shown from observations in Chen et al. (2002).

observations (the triplet S I lines commonly used for chemical abundance determination are located around 6756 Å).

Stellar parameters and elemental abundances are derived using the data-driven approach of The Cannon (Ness et al. 2015) which first uses a training sample to derive several stellar labels that are to be propagated to the entire sample (see Buder et al. 2018 for the details). The training sample was analysed using SME (Spectroscopy Made Easy, Valenti & Piskunov 1996; Piskunov & Valenti 2017) that performs spectrum synthesis with 1D LTE (Local Thermal Equilibrium) hydrostatic stellar atmosphere MARCS models. It is important to mention that GALAH DR2 incorporates non-LTE line formation for several elements using departure coefficients from LTE. In respect to our study, O (Amarsi et al. 2016a), Mg (Osorio et al. 2015), Si (Amarsi & Asplund 2017) and Fe (Amarsi et al. 2016b) are corrected for 1D non-LTE.

We selected only dwarf stars ($T_{\rm eff}$ > 5000 and log g > 4.0) that have a good parameter flag value from *The Cannon* (`flag_cannon == 0`). At this point, we select for each element only the stars for which *The Cannon* gives a good abundance flag (`flag_x_fe == 0`): this leads to a sample of 142 000 stars with good O abundance, 27 638 stars for C, 148 765 for Mg, and 121 105 for Si.

The fact that so few stars from the original sample have good C abundances is caused by the combination of detection limits and the flagging algorithm of *The Cannon*. In fact, only one C line is used for the abundance determination (at 6588 Å) and only a small training sample for C is available (see Table 2 in Buder et al. 2018).

We then grouped the stars selected for each element in metallicity bins of 0.1 dex, as shown in Fig. 1, determining the mean value and dispersion of the ratio of [X/H] in each bin, where X is C, O, Mg, and Si. It is clear from Fig. 1 that the assumption of scaling all the [X/H] (with X one of the element in this study) as [Fe/H] is not correct, especially for stars in the more metal-poor and metal-rich regime of our metallicity range. The trends of [X/H] vs. [Fe/H] for the stars selected in this study are presented in Fig. A.1.

Even if our values are corrected for non-LTE, it is important to remember that they are based on 1D models. Recent new determinations for non-LTE values have been derived using 3D model atmospheres. In this respect, Amarsi et al. (2019) show new abundances for C, O, and Fe corrected for 3D non-LTE for 187 F and G stars in the Galactic disc and halo. It seems that even if the corrections for O are more severe in the metal-rich regime, the correction from our 1D non-LTE values should not be substantial because our sample is made of dwarf stars, where this effect is not that large.

As previously stated, there are no S abundance determinations from GALAH and we assume that it scales as Si as shown in Chen et al. (2002). The same trend is present in several studies (Caffau et al. 2005; Jönsson et al. 2011; Takeda et al. 2016; Duffau et al. 2017) regarding dwarfs and giants, reassuring us that it's possible to scale S with the Si abundance trends.

2.2. Chemical model

In order to account for the chemical composition of the planet, we include only the major rock- and ice-forming species. The mixing ratios (by number) of the different species as a function of the elemental number ratios is denoted by X/H and corresponds to the abundance of element X compared to hydrogen for solar abundances, which we take from Asplund et al. (2009) and are given as follows: He/H = 0.085; C/H = 2.7×10^{-4}; O/H = 4.9×10^{-4}; Mg/H = 4.0×10^{-5}; Si/H = 3.2×10^{-5}; S/H = 1.3×10^{-5}; and Fe/H = 3.2×10^{-5}.

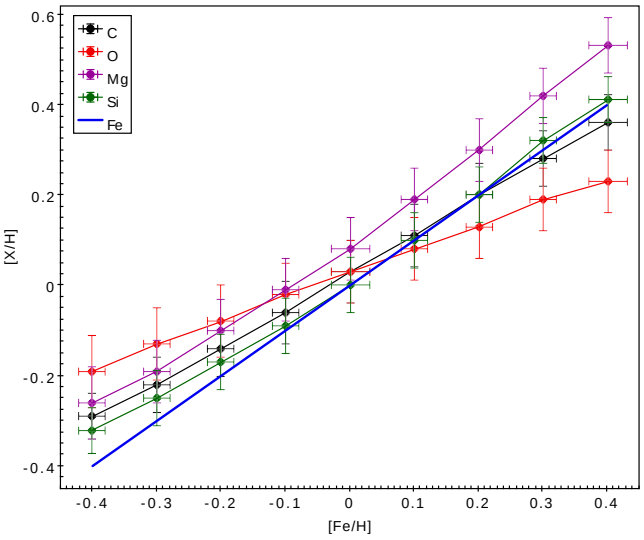

Fig. 1. Stellar abundances of Mg, Si, O, and C as function of [Fe/H] for the stars in our sample. The stellar abundances have been observed in the GALAH survey (Buder et al. 2018). The error bars are the mean deviations of the observations. The data is given in Table A.1. Sulfur (not shown) scales in the same way as silicon (Chen et al. 2002).

These different elements can combine for different molecular species. We list these species, as well as their condensation temperature and their volume mixing ratios $v_{\rm Y}$, in Table 1. More details on the chemical model can be found in Madhusudhan et al. (2017) and Bitsch et al. (2018a).

To account for different host star metallicities, we scale the solar values from Asplund et al. (2009) with the corresponding scaling from Fig. 1. In addition, sulfur scales the same as silicon (Chen et al. 2002).

As we focus on solid formation close to the water ice line, the solids in our simulation still form at temperatures larger than 70 K, meaning that CO, CH_4, and CO_2 are in gaseous form and, they, thus do not contribute to the solid planetary building blocks. However, including the gaseous CO and CO_2 binds a lot of oxygen, which is then not available to form water ice, in contrast to the study by Santos et al. (2017) and Cabral et al. (2019). This binding of oxygen can greatly reduce the amount of available water around stars with high C/O ratios. We discuss how the amount of carbon bound in molecules that do not bind any oxygen (e.g. methane) influences our results in Appendix B.

2.3. Planet formation

As outlined in the introduction, the formation of super-Earths can happen through many different formation channels. However, all core accretion theories agree that solid material, either in the form of pebbles or planetesimals (for a review, see Johansen & Lambrechts 2017), must be accreted to reach masses of a few Earth masses. In this work, we focus on the elemental and solid composition of planetary building blocks formed completely interior ($T > 150$ K) and completely exterior ($T < 150$ K) to the water ice line before applying it to a planet formation model. In principle, growing planets migrate through the disc (for a review, see Baruteau et al. 2014), but accretion, especially in the pebble accretion scenario, can easily be fast enough that the planet is fully grown before it starts to migrate significantly

Table 1. Condensation temperatures and volume mixing ratios of the chemical species.

Species (Y)	$T_{\rm cond}$ [K]	$\upsilon_{\rm Y}$
CO	20	0.45 × C/H
CH_4	30	0.45 × C/H
CO_2	70	0.1 × C/H
H_2O	150	O/H - (3 × $MgSiO_3$/H + 4 × Mg_2SiO_4/H + CO/H + 2 × CO_2/H + 3 × Fe_2O_3/H + 4 × Fe_3O_4/H)
Fe_3O_4	371	(1/6) × (Fe/H - S/H)
FeS	704	S/H
Mg_2SiO_4	1354	Mg/H - Si/H
Fe_2O_3	1357	0.25 × (Fe/H - S/H)
$MgSiO_3$	1500	Mg/H - 2 × (Mg/H - Si/H)

Notes. Condensation temperatures for molecules are taken from Lodders (2003). For Fe_2O_3 the condensation temperature for pure iron is adopted (Lodders 2003). Volume mixing ratios $\upsilon_{\rm Y}$ (i.e. by number) are adopted for the species as a function of disc elemental abundances (see e.g. Madhusudhan et al. 2014). We note that the Mg abundance is always larger than the Si abundance.

(Bitsch et al. 2015b). However, in reality, planets formed exterior to the water ice line can also cross the water ice line during their assembly, which allows them to have a lower water content compared to planets formed completely exterior to the water ice line (Bitsch et al. 2019b), which can help to explain the formation of the Trappist-1 system (Schoonenberg et al. 2019). The planetary composition in this case is just a mixture between the composition acquired exterior and interior to the water ice line. We show in Sect. 4 and Appendix C the results of simple planet formation model including pebble accretion, disc evolution and planet migration. The final water ice content of planets in this model is directly correlated to the temperature at which the solids are accreted and is as such always a mixture between the minimum and maximum allowed water ice content of the model, which we discuss in Sect. 3.

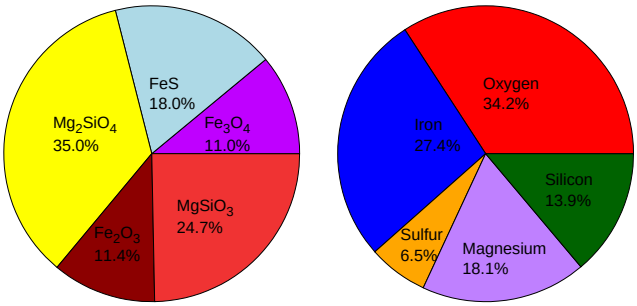

Fig. 2. Solid (*left*) and elemental mass fractions (*right*) of solid planetary building blocks formed completely interior to the water ice line ($T > 150$ K) around a star with [Fe/H] = 0. The mass of the building blocks is dominated by Mg_2SiO_4 and $MgSiO_3$, while the elemental masses are dominated by oxygen and iron, making up around 60% of the total mass of the planet.

3. Composition of solid planetary building blocks formed completely interior or exterior to the water ice line

In this section, we show the elemental and solid composition of solid planetary building blocks formed entirely interior or exterior to the water ice line (but interior to the CO_2 ice line) to give an overview of the extreme cases. We then apply the same chemical model in Sect. 4 and study the compositions of planets that grow by pebble accretion and migrate through the disc, where they can cross the ice lines. We first discuss the elemental and solid composition of solids formed at [Fe/H] = 0 and then move on to lower and higher [Fe/H] values. We then summarize the findings in Figs. 10 and 11.

3.1. Solar metallicity

In Fig. 2, we show the solid and elemental mass fractions of solid planetary building blocks formed entirely interior to the water ice line ($T > 150$ K) at [Fe/H] = 0.0. The mass of the solid planetary building blocks on a molecular level is dominated by Mg_2SiO_4 and $MgSiO_3$, while the elemental masses are dominated by oxygen and iron.

The total elemental masses from our chemical model are similar to the Earth's abundance (McDonough & Sun 1995), however, our model shows a larger magnesium fraction compared to the Earth. This is related to the usage of the magnesium abundance from the Galactic abundances at [Fe/H] = 0, which is larger than the solar values. This results in an overabundance of magnesium for our planetary composition. If we instead use directly the solar abundances (Asplund et al. 2009) our model is much closer to the Earth's composition but it does not match exactly. We attribute these differences to our simple chemical model which only traces the main carriers of material. In addition, our formation model does not account for the impact history on Earth, where impactors originated from different regions in the solar system.

In Fig. 3, we show the solid and elemental mass fractions of solid planetary building blocks that formed entirely exterior to the water ice line ($T < 150$ K). The solid mass is now mainly dominated by water ice (H_2O) and, thus, oxygen. The total elemental composition, then, is obviously not Earth like at all, confirming that the Earths did not form exterior to the water ice line even though the water ice line can evolve interior to 1 AU during the evolution of the protoplanetary disc (Oka et al. 2011; Bitsch et al. 2015a). In the pebble accretion scenario, this problem could be solved by the growth of Jupiter that blocks the

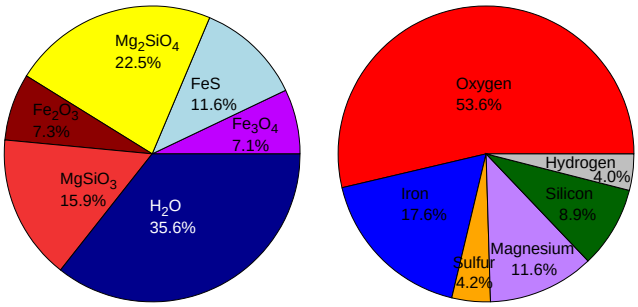

Fig. 3. Solid (*left*) and elemental mass fractions (*right*) of solid planetary building blocks formed completely exterior to the water ice line ($T < 150$ K) around a star with [Fe/H] = 0. The solid level is dominated by H_2O and Mg_2SiO_4, while oxygen and iron clearly dominate the elemental composition, making up nearly 70% of the planetary mass.

inflow of water-rich particles into the inner disc (Morbidelli et al. 2016) even though the water ice line sweeps interior to 1 AU after 1 Myr, according to viscous disc evolution models (Oka et al. 2011; Bitsch et al. 2015a; Baillié et al. 2015).

3.2. Sub-solar metallicities

In Fig. 4, we show the solid and elemental mass fractions of solid planetary building blocks formed entirely interior to the water ice line ($T > 150$ K) around stars with sub-solar [Fe/H]. The overall solid and elemental abundances are very similar to solids formed around stars with [Fe/H] = 0. This is caused by very similar slopes in the abundance trends for silicon, magnesium, iron, and sulfur (Fig. 1). Oxygen, on the other hand, is overabundant compared to the other elements, which has no influence on the amount of the major rock-forming species (Mg_2SiO_4, FeS, Fe_3O_4, Fe_2O_3 and $MgSiO_3$) in our chemical model. Thus the composition of solids formed interior to the water ice line around stars with sub-solar metallicity is very similar to stars formed around solar metallicity.

In Fig. 5 we show the solid and elemental abundances of solid planetary building blocks formed exterior to the water ice line ($T < 150$ K) for sub-solar metallicities. For lower and lower [Fe/H], water ice becomes more and more dominant for the total mass budget of the solids and with it, oxygen. This is clearly related to the fact that the oxygen abundances is enhanced compared to the other elements at low [Fe/H], see Fig. 1. In our chemical model, this implies that the relative abundances of rock-forming materials are similar to stars with [Fe/H] = 0 but the iron content decreases for lower overall metallicities. This is related to the overabundance of oxygen allowing for the formation of more H_2O which becomes, thus, more and more dominant for lower [Fe/H]. As a consequence, the water ice fraction in the solid planetary building blocks can be above 50% for [Fe/H] = −0.4.

3.3. Super-solar metallicities

In Fig. 6, we display the solid and elemental mass fractions of solid planetary building blocks formed interior to the water ice line ($T > 150$ K) around stars with super-solar metallicity. As can be seen from Fig. 1, the magnesium abundance increases strongest with [Fe/H], resulting in an overall increase of Mg_2SiO_4 in the mass fraction of the formed solids. However, the overall mass fractions for the different elements only changes slightly, because the relative mass of Mg and O inside of the

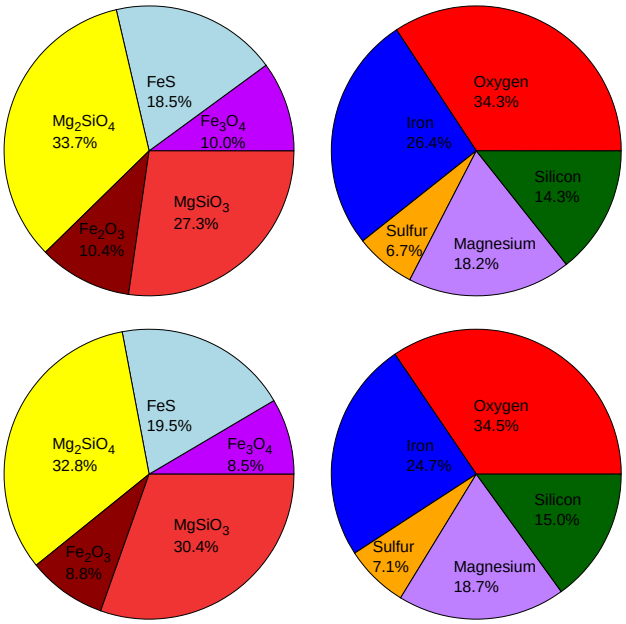

Fig. 4. Solid (*left*) and elemental mass fractions (*right*) of solid material formed completely interior to the water ice line ($T > 150$ K) around a star with [Fe/H] = −0.2 (*top*) and [Fe/H] = −0.4 (*bottom*). As for [Fe/H] = 0 (Fig. 2), the solid composition is dominated by Mg_2SiO_4 and $MgSiO_3$, while the elemental composition is dominated by oxygen and iron, making up around 60% of the total mass of the planet.

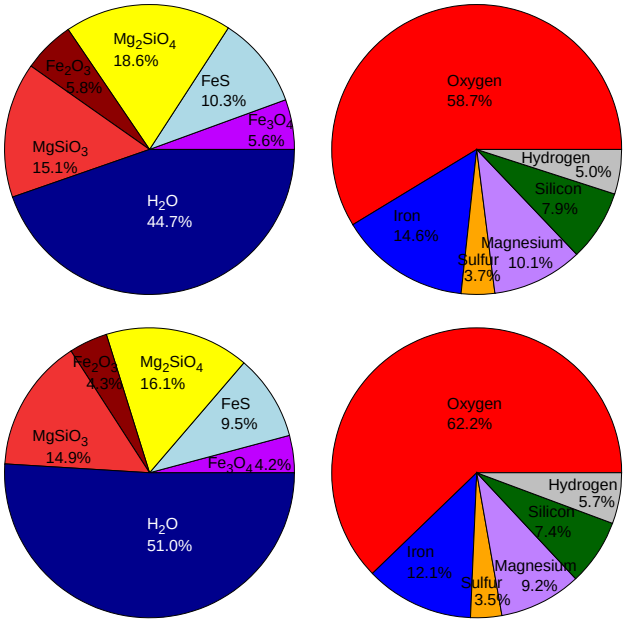

Fig. 5. Solid (*left*) and elemental mass fractions (*right*) of solid planetary building blocks formed completely exterior to the water ice line ($T < 150$ K) around a star with [Fe/H] = −0.2 (*top*) and [Fe/H] = −0.4 (*bottom*). As for [Fe/H] = 0 (Fig. 2), the solid composition is dominated by H_2O, while the elemental composition is dominated by oxygen and iron, where the iron content decreases for lower overall metallicities.

rock-forming compounds $MgSiO_3$ and Mg_2SiO_4 changes only slightly as well, leaving the overall elemental trend with [Fe/H] quite constant.

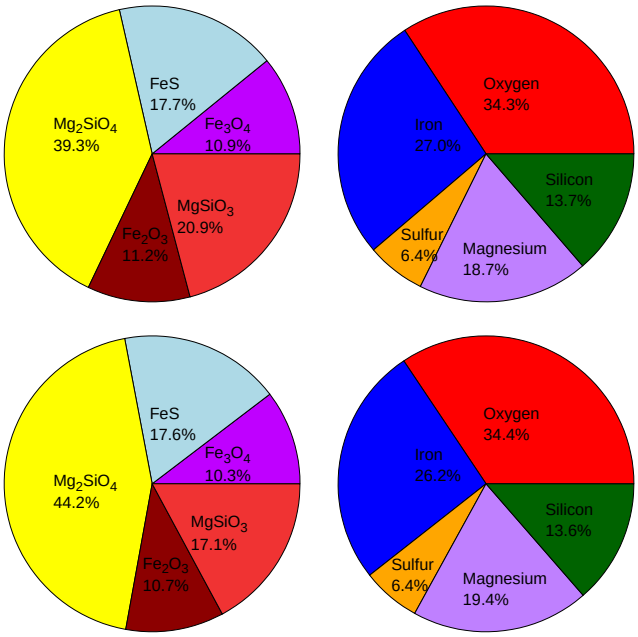

Fig. 6. Solid (*left*) and elemental mass fractions (*right*) of solid planetary building blocks formed completely interior to the water ice line ($T > 150$ K) around a star with [Fe/H] = +0.2 (*top*) and [Fe/H] = +0.4 (*bottom*). As for [Fe/H] = 0 (Fig. 2), the solid composition is dominated by Mg_2SiO_4 and $MgSiO_3$, while the elemental composition is dominated by oxygen and iron, making up around 60% of the total mass of the planet, as for all [Fe/H] values.

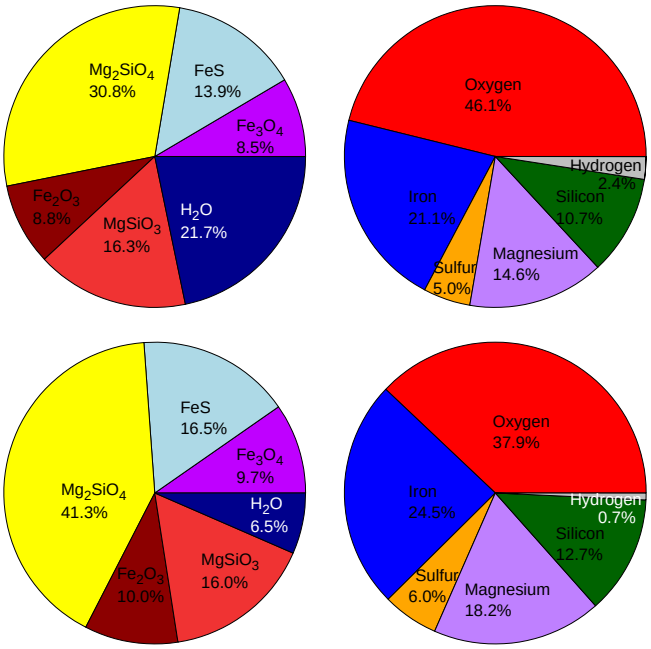

Fig. 7. Solid (*left*) and elemental mass fractions (*right*) of solid planetary building blocks formed completely exterior to the water ice line ($T < 150$ K) around a star with [Fe/H] = +0.2 (*top*) and [Fe/H] = +0.4 (*bottom*). In contrast to the mass fractions of solids formed around lower metallicity stars exterior to the water ice line, the dominant solids mass is not water ice, but Mg_2SiO_4. In fact, the water ice content is reduced to just a few percent for solids formed around stars with [Fe/H] = 0.4. The dominant elemental mass fraction is oxygen and iron, however the oxygen fraction is not as elevated as for planets formed around stars with low [Fe/H], see Fig. 5.

Additionally, the oxygen abundance is reduced compared to the other elements but there is still enough oxygen to fully oxidize iron, magnesium and silicon. This implies that the reduction of the oxygen abundance relative to the other elements has no influence on the elemental composition of solids formed entirely interior to the water ice line. If the galactic trends for these elements continue for even larger [Fe/H] abundances, we expect a deviation from the derived mass fractions of the elements inside the solids formed interior to the water ice line here because there might not be enough oxygen available to fully oxidize Fe, Mg, and Si.

In Fig. 7, we show the elemental and solid mass fractions of solid planetary building blocks formed entirely exterior to the water ice line ($T < 150$ K) around stars with super-solar metallicity. In contrast to solids formed around stars with low [Fe/H] exterior to the water ice line (e.g. Fig. 5, where the water ice fraction of the solids decreased dramatically). In fact for [Fe/H] = 0.4, the water ice mass fraction is only of a few percent.

The low water ice mass fraction is caused by the reduced oxygen abundances compared to the C, Si, Mg, Fe, and S abundances around stars with large [Fe/H]. For more, see Fig. 1. This lower oxygen abundance still allows for Si, Mg, and Fe to be fully oxidized, binding a lot of oxygen. In addition, the large carbon abundance (Fig. 12) binds a lot of oxygen into CO and CO_2, leaving very little oxygen that can then form water ice (see Table 1). This results in a very low water ice abundance in solids formed exterior to the water ice line around metal-rich stars. As a consequence, the elemental abundances show an increase of Fe, S, Mg, and Si, along with a reduction of H and O, with increasing [Fe/H] due to the reduced availability of water ice. If the same trend for all elements holds true for even larger [Fe/H], our chemical model predicts that water ice would not be available at overall higher metallicities than [Fe/H] > 0.4.

4. Planet formation

In this section, we show the results of a simple planet formation model based on pebble accretion to study the final position, masses, and water ice content of formed planets. The details of the planet formation model are given in Appendix C and follow standard models used in the past (e.g. Bitsch et al. 2015b). Our model contains a decreasing pebble flux with time, along with an evolving protoplanetary disc model which cools in time, meaning that the ice lines move inward in time and type-I migration for the growing planetary cores. We start our planetary embryos with 0.01 Earth masses. The growth of the planets stops at the pebble isolation mass, which is when planets start to open a small gap in the protoplanetary discs, halting the inward flux of pebbles and, thus, accretion (Lambrechts et al. 2014; Bitsch et al. 2018b). We do not include gas accretion and type-II migration because our work focuses on the solid composition of material and, thus, our planet formation model focuses on the formation of super-Earths.

Past simulations have shown that the water ice content in the protoplanetary disc can greatly influence the disc structure and the planet formation pathway regarding growth and migration (Bitsch & Johansen 2016). However, constructing a detailed disc model based on the different abundances is beyond the scope of this work. We therefore rely on the disc model derived for solar metallicities presented in Bitsch et al. (2015a) and use this for all our simulations. This approach might not be as accurate, but it allows for an easy comparison between the different scenarios, because the planet migration rates are the same due to the same disc model.

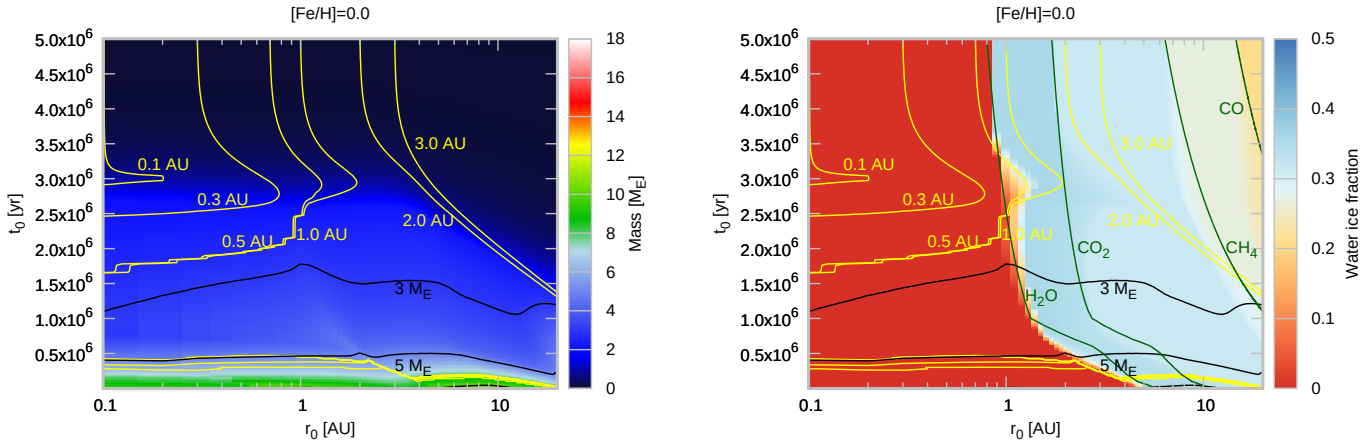

Fig. 8. Final planetary masses (*left*) and final water ice content (*right*) of the planets formed in our simulations as function of the planetary starting position r_0 and starting time in the disc t_0 around a star with [Fe/H] = 0.0. Yellow lines indicate the final planetary positions in AU after 5 Myr and black lines mark the final planetary masses in Earth masses. Green lines in the *right panel* mark the ice lines of H_2O, CO_2, CH_4 and CO. Planets forming very early in the disc migrate all the way down to 0.1 AU. The majority of planets are trapped in the region of outward migration until the end of the disc's lifetime. The decrease in the water ice fraction at large initial distances is caused by the accretion of CO_2, CH_4, and CO into the planet, which reduces the relative water ice fraction of the planet, but increases the total ice fraction of the planet.

4.1. Solar metallicity

In Fig. 8, we show the final planetary mass (left) and the corresponding water ice content of the planets (right) as function of the starting position r_0 and starting time t_0 of the planet in the disc around a star with [Fe/H] = 0 at the final time of 5 Myr. The yellow and black lines mark the final planetary position and masses, while the green lines mark the ice lines of H_2O, CO_2, CH_4 and CO.

Planets growing in the early stages of the disc (small t_0) receive the largest pebble flux and thus grow fastest. In addition, in the early stages of the disc evolution, the pebble isolation mass, at which pebble accretion stops, is highest (e.g. Bitsch et al. 2015b, 2019b). This results in the most massive planets that can reach masses of up to 5–10 Earth masses within this model ($t_0 < 500$ kyr). Due to the model-choice of a constant Stokesnumber for the pebbles, pebbles are much smaller in the outer disc where the gas density is lower, reducing the pebble accretion rate for planets further away from the star.

As the pebble flux decreases in time, the planetary growth rate is reduced. Additionally, the disc cools and its aspect ratio is reduced, resulting in a smaller pebble isolation mass at later times. Thus, planets formed at large initial times t_0 grow slower and to lower masses than planetary embryos injected at earlier starting times.

During their growth process, the planets migrate through the disc. The disc model we used (Bitsch et al. 2015a) features a region of outward migration exterior to the water ice line where planets can be trapped as they grow. These planets could then only be released from the disc when the disc dissipates and the region of outward migration can only hold small planets (Bitsch et al. 2015a). As a result, nearly all of the planets in our simulations are trapped exterior to 0.1 AU, which is the inner edge of our disc model.

However, planetary systems most likely contain more than one planet, which then results in a different dynamical history of the system. The N-body simulations of Izidoro et al. (2019) and Bitsch et al. (2019a) use the same disc model and show that planetary embryos can migrate inwards in a convoy. This is caused by the mutual interactions between the bodies which increase their eccentricity. An increase in the planetary eccentricity quenches the entropy-driven corotation torque (Bitsch & Kley 2010) which results in the inward migration of these planets. As a consequence, multiple planetary embryos that grow exterior to the water ice line can migrate all the way to the inner edge in a convoy (Izidoro et al. 2019), in contrast to the single planetary embryos used in the work presented here. Hence, we think that the final semi-major axes of the planets in our simulations might be different if multi-body simulations are used, however, the growth of these embryos by pebble accretion is very fast and, thus, local so that the water ice content is not affected much by the multiplicity (Izidoro et al. 2019).

The planets that grow entirely exterior to the water ice line and are trapped until they reach the pebble isolation mass have the largest water ice content, as shown by Bitsch et al. (2019b). The water ice content of the planets that formed completely interior to the water ice line is by construction zero, while the water ice content is largest for planets formed just exterior to the water ice line. Planets forming even further away from the water ice line have a lower water ice content, because these planets might accrete CO_2, CH_4, and CO, reducing the relative mass fraction of water ice. However, these planets would have a higher ice fraction. In fact the water ice content of planets formed just exterior to the water ice line and planets formed completely exterior to the CO ice line differ by about a factor of two. The planets formed far away from the star are dominated in CO_2, CH_4 and, CO ice instead of water ice. As expected, the water ice content of the planets is between the maximal allowed value (Fig. 3) and zero.

Another factor that can influence the water ice content of the formed planets is the direction of migration. Bitsch et al. (2019b) showed that planets have a lower water ice content in a scenario where planets can only migrate inwards. We see the same effect in our simulations here (see Appendix C).

4.2. Sub- and super-solar metallicity

In Fig. 9, we show the final masses, positions and water ice fractions of planets formed at different initial distances r_0 and at different initial times t_0 around stars with sub- and super-solar metallicity. The exact elemental abundances for each [Fe/H] value are shown in Fig. 1 and Table A.1.

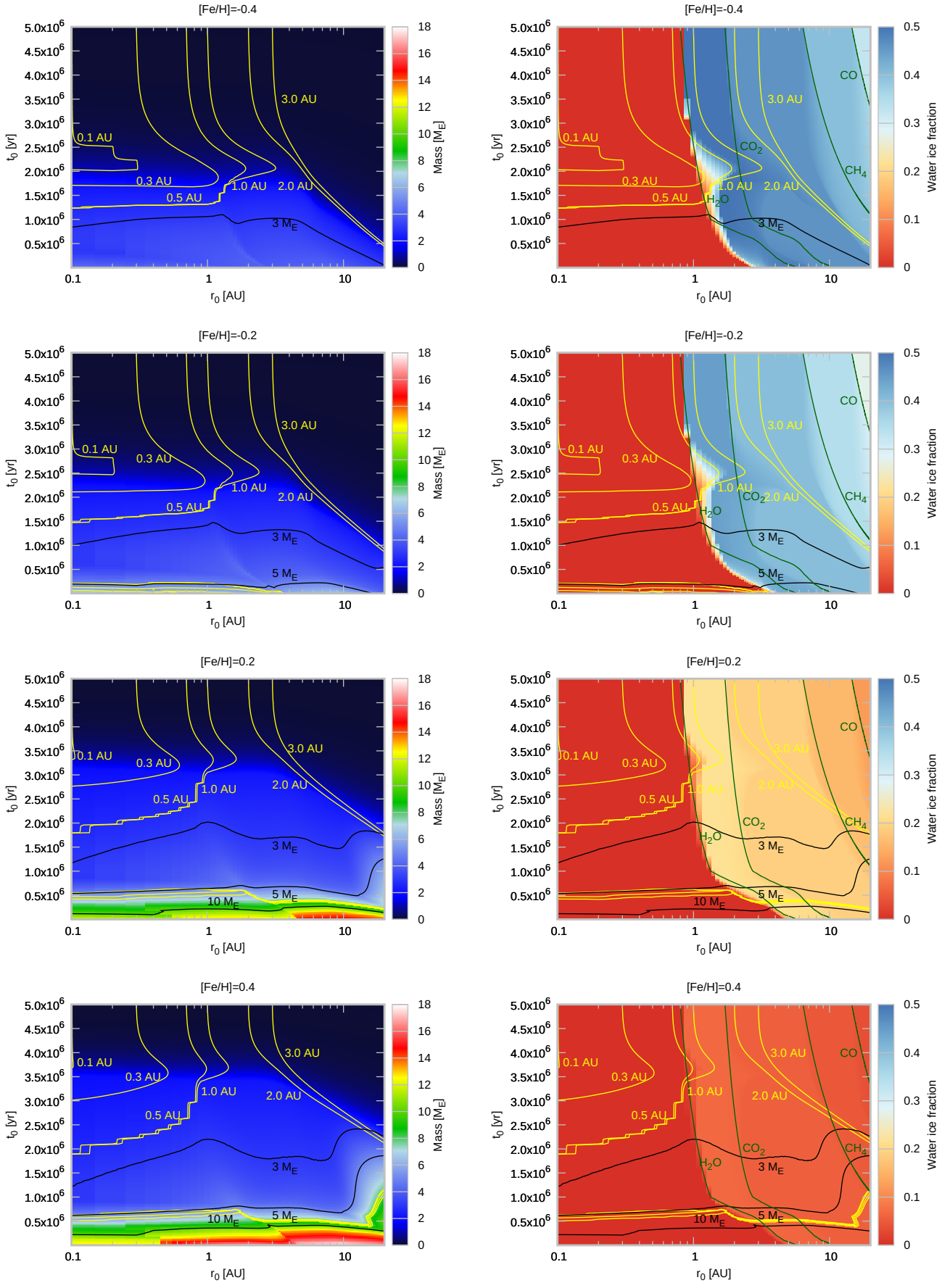

Fig. 9. Same as in Fig. 8, except that the planets are formed around stars with different [Fe/H] values and thus chemical abundances for the all elements (Fig. 1). Stellar abundances increase from top to bottom. As the stellar abundances increase, the water ice content of the planet decreases due to the lack of water ice as a result of the increasing C/O ratio (Fig. 12).

Two effects for increasing host star metallicity are immediately clear from Fig. 9: (i) the planetary masses increase with increasing [Fe/H] and (ii) the water ice content of the planets decreases with increasing [Fe/H]. Both effects are not surprising. The increasing planetary masses with [Fe/H] are simply related to the higher pebble flux at larger [Fe/H], which allows for faster accretion and, as a result, the planets can reach the pebble isolation mass earlier, when the pebble isolation mass is still large. The reduced water ice content with increasing [Fe/H] is simply related to the overall reduced water ice abundance at higher [Fe/H] from our chemical model.

There are, however, some other small differences for the planet formation pathway. In cases of low metallicity, the planets grow very slowly, meaning that they just reach 2–3 Earth masses. Planets of that mass range are trapped in the region of outward migration until disc dissipation at 5 Myr and, thus, they do not migrate to the inner edge. As a consequence, at low [Fe/H], there is basically no planet reaching the inner edge in our disc model. However, chains of multiple planets can migrate inwards due to their mutual increase in eccentricity, which reduces outward migration due to the entropy-driven corotation torque (Bitsch & Kley 2010; Izidoro et al. 2017, 2019). If the metallicity is slightly larger ([Fe/H] > -0.2), some planets become larger than 5 Earth masses, which allows them to migrate to the inner edge of the disc towards the end of the disc's lifetime (Planets below the yellow lines at low t_0 in Fig. 9 migrate all inwards to 0.1 AU).

As already shown in Fig. 8, the water ice content of the planets is reduced if they are formed further away and the water ice content of the planets formed close to the water ice line is largest. This is, as stated before, caused by the fact that the planets formed exterior to the CO_2, CH_4, or CO ice line accrete these ices as well. As a result the water ice content of the planet decreases but the total ice fraction can increase (not shown).

The total water ice content of the planets formed in the simulations is between the maximal amount of water allowed by the chemical model for a given stellar composition (see Fig. 10) and zero. Planetary migration across the water ice line can reduce the water ice content of growing planets. For more, see Appendix C. In particular, if planetary migration is only directed inwards, the water ice content can be reduced compared to a scenario where planet migration is outwards at the water ice line (Bitsch et al. 2019b). Nevertheless, the highest water ice content of planets can be achieved at low host star metallicity due to the lowest C/O ratio, which allows for the largest water ice content, independently of whether migration is taking place inwardly or outwardly.

5. Discussion

In Figs. 10 and 11, we show the solid and elemental mass fractions of solid planetary building blocks formed interior ($T > 150$ K) and exterior ($T < 150$ K) to the water ice line as a function of [Fe/H]. These figures summarize the trends described in Sect. 3 to give a better overview over the trends. In addition we show in Fig. 12 the C/O ratio as function of [Fe/H]. In the following, we discuss the assumptions and implications of the results of our model on planet formation, where we also show the results of a planet formation model in Appendix C.

5.1. Planet formation

One of the main questions in planet formation theories is where the first planetesimals and planetary embryos formed which then went on to develop into fully-grown planets. In recent years, the water ice line has become the prime suspect for where the first planetesimals may have formed (Ida & Guillot 2016; Drążkowska & Alibert 2017), also because of the large water abundance in the Solar System (Lodders 2003). The condensation of water onto grains allows them grow larger than with pure coagulation (Ros & Johansen 2013; Schoonenberg & Ormel 2017; Ros et al. 2019), which allows planetesimals to form more easily. This is caused by larger particle sizes, which allow gravitational collapses of pebble clouds to planetesimals at lower overall metallicities (Yang et al. 2017). In contrast, the CO ice line is not thought to harbour the same effect as the water ice line because the grains drift inwards faster than they can grow through condensation at these distances (Stammler et al. 2017).

However, all these simulations were conducted with solar abundances of water and CO. As the host star metallicity increases, our model predicts a significant reduction in water (Fig. 10, along with an increase in CO as shown in Fig. 12). A change in the water ice fraction has significant implications for the formation of planets around the water ice line (Bitsch & Johansen 2016).

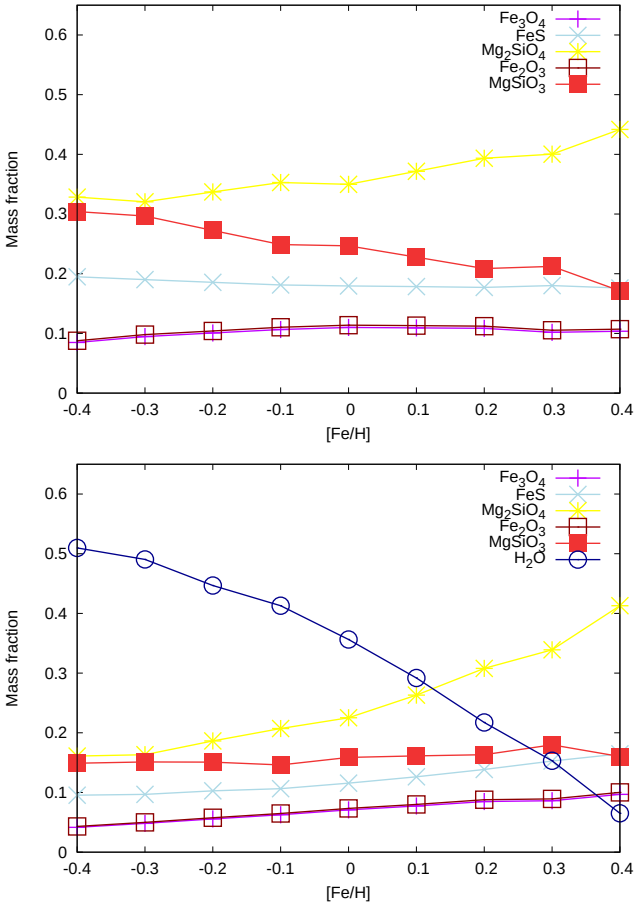

Fig. 10. Solid mass fractions of solid planetary building blocks formed completely interior (*top*) to the water ice line and completely exterior (*bottom*) to the water ice line as function of [Fe/H]. The lines of Fe_2O_3 and $MgSiO_3$ are overlapping because the mass fraction of these solids is very similar. For solids formed interior to the water ice line, a clear rise in the Mg_2SiO_4 fraction and decline in the $MgSiO_3$ fraction is visible, caused by the increase of Mg/Si for increasing [Fe/H]. Solid planetary building blocks formed exterior of the water ice line show a clear trend of reduced water ice fraction with increasing [Fe/H], which is then compensated by an increase in Mg_2SiO_4.

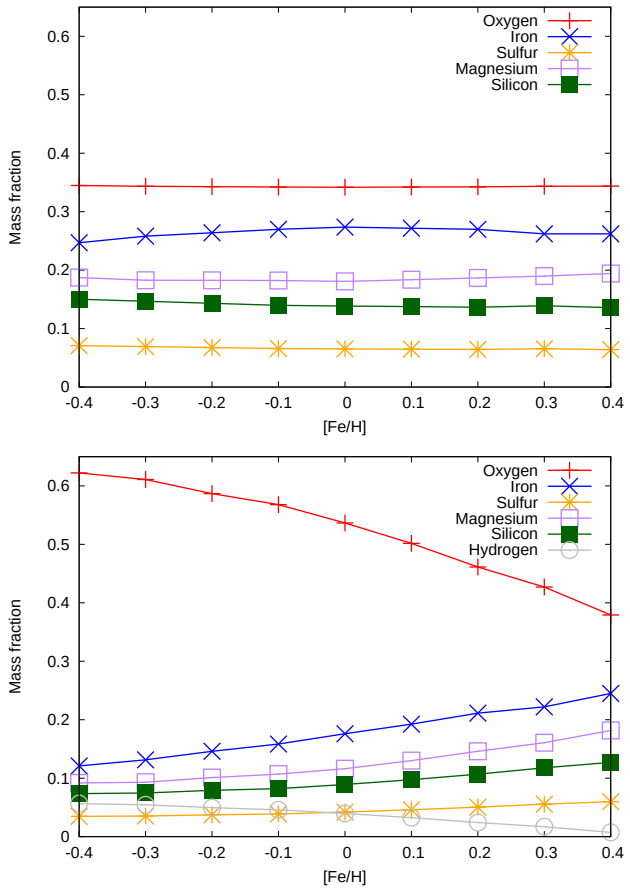

Fig. 11. Elemental mass fractions of solid planetary building blocks formed completely interior (*top*) to the water ice line and completely exterior (*bottom*) to the water ice line as function of [Fe/H]. The elemental abundances of solids formed interior to the water ice line ($T > 150$ K) are roughly constant for all values of [Fe/H]. In contrast, the oxygen content inside the solids severely decreases for solids formed exterior to the water ice line ($T < 150$ K) due to the reduced oxygen abundances relative to C, Si, Mg, Fe and S for increasing [Fe/H].

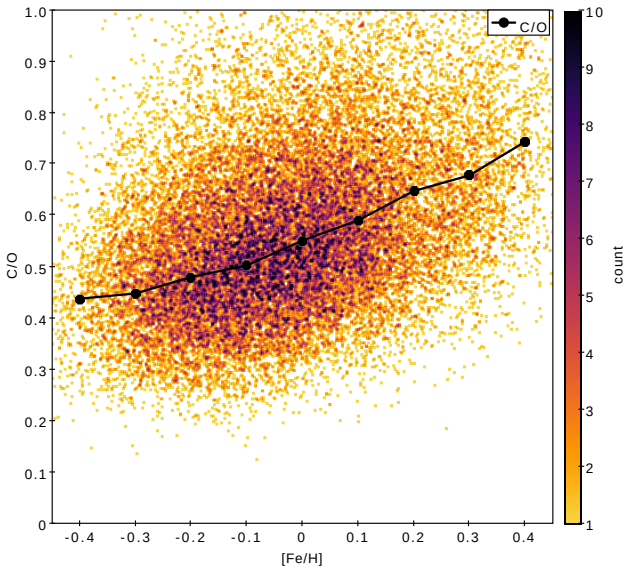

Fig. 12. C/O ratio as function of [Fe/H] with the stars containing good carbon and oxygen values from the GALAH survey. Black line originates from the data shown in Fig. 1 and marks the mean C/O ratio from all stars in our sample. The number of the stars shown here is less than was used to derive the [C/H] and [O/H] value in Fig. 1 because stars with good carbon value might not have a good oxygen value at the same time. As [Fe/H] increases, so does the C/O ratio. This implies that more oxygen can be bound with carbon to form CO and CO_2 for increasing [Fe/H].

In the case of low host star metallicity, the water ice fraction is much larger than for solar metallicity, which could increase the effects of condensation and could allow grains to grow larger. This could significantly help planet formation around the ice line in low-metallicity environments, where building blocks are rare, but the increased pebble sizes due to condensation allow for an easier collapse of pebble clouds to planetesimals (Yang et al. 2017). However, this effect might be counteracted by the overall low metallicity which hinders the gravitational collapse of pebble clouds to planetesimals as well (Yang et al. 2017). This implies that the effect of condensation cannot be so strong that giant planet cores grow quickly and easily due to the lack of giant planets around low-metallicity host stars (Santos et al. 2004; Fischer & Valenti 2005; Johnson et al. 2010). Additionally, it could imply that super-Earths formed around low-metallicity stars could be water-rich, in contrast to super-Earths formed around high-metallicity stars, where water ice is rare.

On the other hand, the water ice fraction is very low around stars with super-solar metallicity, which implies that maybe condensation is not the main driver of grain growth and, thus, planetesimal formation around these stars. Condensation at the water ice line is reduced but it could be compensated by the overall increased metallicity around these stars, which can trigger planetesimal formation (see Johansen et al. 2014 for a review). The simulations of Yang et al. (2017) show that even small particles with Stokes numbers around 10^{-3} can trigger planetesimal formation, if the overall metallicity is super-solar, indicating that the contribution of condensation to particle growth is not necessarily required to form planetesimals.

The occurrence rate for giant planets increases with host star metallicity (Santos et al. 2004; Fischer & Valenti 2005; Johnson et al. 2010), which is confirmed by many simulations in the core accretion scenario (Ida & Lin 2004; Mordasini et al. 2009; Bitsch & Johansen 2017; Ndugu et al. 2018). However, these simulations do not take into account the effects of different elemental scalings with host star metallicity and should be revisited given the effects found in this study. In addition, the amount of CO and CO_2 around these stars is increased in comparison to stars with solar abundances that are due to their elevated C/O ratio (Fig. 12). This could allow condensation at the CO snow line to outperform radial drift, implying that giant planet formation around stars with solar and sub-solar metallicity starts at the water ice line, where condensation can increase the pebble sizes, while giant planet formation around high-metallicity stars could start at the CO ice line, where our model predicts a larger amount of CO available for for condensation compared to solar and sub-solar metallicity. This, however, needs to be tested with future models, such as that of Drążkowska & Alibert (2017), which combines grain growth and drift with condensation and planetesimal formation. In addition the C/O ratio of giant planet host stars could help to distinguish if water ice condensation is the main driver of giant planet formation.

5.2. Composition of super-Earths and gas giants for different host star abundances

In our model, we study the composition of solid material around host stars with different metallicities. We use this model to

calculate the composition of solid planetary building blocks that form interior or exterior to the water ice line. In Sect. 4, we show the water ice content of planets using a planet formation model featuring planet migration, disc evolution, and pebble accretion, which resulted in water ice contents of the formed planets established between zero and the maximal content allowed for the specific host star abundance. In Appendix C, we explain our planet formation model in detail. Our planet formation simulations coupled to our chemical model shows that the water ice content of the super-Earths is between zero and the maximal allowed water content of the model (Figs. 9 and 10). This result is consistent with other simulations of planet formation including compositions and planet migration (Alessi et al. 2017; Bitsch et al. 2019b).

In Fig. 10, we show the mass fraction that contribute to solid planetary building blocks for changing host star metallicities. For planets forming completely interior to the water ice line ($T > 150$ K), the composition of the solids only changes slightly, with an increase of Mg_2SiO_4 by about 15% from [Fe/H] = −0.4 to 0.4, while $MgSiO_3$ decreases by the same amount over the same range of [Fe/H]. This is caused by the relative stronger increase of magnesium compared to silicon, with [Fe/H]. For more, se Fig. 1. In the elemental mass fraction of the solids (Fig. 11), on the other hand, the relative mass fractions of all elements stay roughly constant with [Fe/H]. This is caused by a very similar oxygen and magnesium fraction inside of $MgSiO_3$ and Mg_2SiO_4.

This implies that the overall composition of rocky planets that formed completely interior to the water ice line ($T > 150$ K) is very similar for stars with different metallicity. For rocky planets at solar composition our simulations actually predict a composition that is very close to the Earth (McDonough & Sun 1995). On the other hand, some super-Earths have densities much higher than the Earth (Guenther et al. 2017), similar to Mercury. These high densities are caused by a large iron fraction, which we do not reach in our model. For Mercury, the high density could be explained by stripping its mantle through a collision, leaving an iron rich remnant (Benz et al. 1988). In simulations that study the formation of close-in super-Earths, collisions are basically inevitable (Ogihara et al. 2015, 2018; Izidoro et al. 2017, 2019; Lambrechts et al. 2019), but collisions are normally treated as perfect mergers in these simulations and, thus, they do not account for mantle stripping. However, this process could help to explain the large densities of some super-Earth planets.

Planets formed completely exterior to the water ice line ($70\,\mathrm{K} < T < 150\,\mathrm{K}$), on the other hand, would show a strong decrease in water ice with increasing host star metallicity (Figs. 10 and C.1). This is caused by the binding of oxygen with carbon to form CO and CO_2, along with the other rock-forming elements, which results in only a small fraction of oxygen that can form water ice. As water ice decreases, Mg_2SiO_4 increases in a similar fashion as for planets formed interior to the water ice line. The elemental trend here gives a clear picture as well (Fig. 11). As the water ice decreases, the oxygen mass fraction decreases and the mass fraction of the other elements increases accordingly.

The consequences for the composition are quite dramatic. Super-Earths formed exterior to the water ice line have a very significant water ice fraction if they form around low-metallicity stars, compared to a very tiny water ice fraction if they form around high metallicity stars (Fig. 9). This has important consequences for the formation mechanism of close-in super-Earths.

In the *Kepler* sample, recent detailed observations have revealed a gap in the radii of the observed super-Earths (Fulton et al. 2017; Van Eylen et al. 2018). This gap is generally interpreted as atmospheric mass loss of small planets either by photo-evaporation (Owen & Wu 2013; Lopez & Fortney 2014) or by mass loss directly from the cooling of the core (Gupta & Schlichting 2019). As a consequence, it is thought that most close-in super-Earths are of mostly rocky nature (Owen & Wu 2017; Jin & Mordasini 2018), putting constraints on planet formation models. However, some models predict that these super-Earths could have water contents up to 10–20% (Gupta & Schlichting 2019), which is in agreement with recent observations (Zeng et al. 2019).

For example, the N-body simulations of Izidoro et al. (2019) show that planets assembled exterior to the water ice line should have a large water ice content (50% in their model), which is mostly inconsistent with the observations. On the other hand, if the assembly of the planets starts exterior to the water ice line, but finishes interior to the water ice line, the final composition could be in line with the observations (Raymond et al. 2018; Bitsch et al. 2019b). For super-Earths formed around high-metallicity stars with [Fe/H] > 0.2, our model predicts a maximum water ice content of 20%, which is naturally consistent with the observed gap in the planetary radius distribution. This could imply that the radius gap could only tell something about the formation channel of super-Earths around stars with [Fe/H] < 0.2. Thus, a more detailed analysis of the host stars within the *Kepler* sample is of crucial importance to constrain planet formation theories.

We applied our model to the solid building blocks of planets and did not focus on the gaseous component of the protoplanetary discs and what this could imply for the composition of giant planets. Giant planets that grow and migrate in protoplanetary discs do not only accrete hydrogen and helium in the gas phase, but heavy elements as well. The accretion of these elements can be enhanced due to the evaporation of volatiles (e.g. H_2O, CO_2, CO) at ice lines (Öberg et al. 2011; Madhusudhan et al. 2017; Booth et al. 2017). As already mentioned, the C/O ratio in the gas phase changes with host star metallicity (Figs. 1 and 12). In addition, hot Jupiters, which are gas giants whose atmosphere we are able to characterize, are more common around high-metallicity stars (Buchhave et al. 2018). This could naturally imply a change in the C/O ratio of the observed giant planet atmospheres compared to solar composition and should be taken into account in the modelling of the planet formation pathway of these planets, where previous simulations were not tailored to match the exact host star abundances (Madhusudhan et al. 2017; Ali-Dib 2017).

5.3. Habitability

Planets that are suspect to harbour life as we know it reside in the habitable zone around their host star (e.g. Seager 2013), which is defined as a region around the star where water could be in liquid form[2]. This implies that a planet inside the habitable zone should actually harbour water. In the Solar System, the Earth formed dry in the inner regions of the protoplanetary disc and water was delivered via impacts of asteroids and comets triggered by the giant planets (Raymond et al. 2009; Raymond & Izidoro 2017). Simulations normally assume a water ice composition gradient around the water ice line, where the most water rich objects can have a substantial amount of water ice. However, around

[2] Life based on other molecules than H_2O could have different habitable zones (Turbo-King et al. 2017).

stars with high metallicity, the water ice fraction is dramatically reduced (Fig. 10), which could have important implications for the potential habitability of planets inside the habitable zone around high-metallicity stars. The study by Abbot et al. (2012), on the other hand, indicates that too much water could actually be potentially dangerous for the habitability of a given planet, implying that planets around stars with a lower metallicity might be more suitable for life. However, as already hinted above, water delivery onto planets is a complicated process that needs much further investigation. Nevertheless, our model suggests that the characterization of potential habitable worlds with future instruments should take the host star composition into account.

5.4. Chemical model

The chemical model we used (Table 1) is a simple equilibrium model that does not take the chemical evolution during the protoplanetary disc stage into account, which can alter the chemical abundances of different molecules (Henning & Semenov 2013; Eistrup et al. 2016). The model we used also does not account for the formation of molecules during the infall stage, however simulations using a solar-like composition (Furuya et al. 2015) seem to be in agreement with our model at solar composition. However, the impact of a more advanced model seems to be much more profound on the gaseous component (Eistrup et al. 2018) and, thus, the planetary atmosphere composition (Cridland et al. 2019) than on the solid composition. However, to calculate the solid composition of the material, the gaseous component also has to be taken into account. This is especially important for the oxygen fraction, as a large fraction of oxygen is bound in CO and CO_2, especially for high C/O ratios.

In the study by Santos et al. (2017), the effect of gas phase CO and CO_2 is not taken into account and they find that the protoplanetary discs should harbour a large water fraction independently of the host star metallicity. This difference between their model, originally presented in Santos et al. (2015), and ours can be attributed to the more detailed chemical model we use. In particular, we include the effects of oxygen binding in CO and CO_2, which binds most of the oxygen, especially for high-metallicity stars with a large C/O ratio (Fig. 12). Additionally, we include the binding of oxygen with iron to form Fe_3O_4 and Fe_2O_3. This results in the low water ice fraction around high-metallicity stars in our model in comparison with the one used by Santos et al. (2017).

As the water ice fraction is closely related to the binding of oxygen with carbon to form CO and CO_2, the water ice fraction would change if a lot of carbon grains would end up bound in molecules that do not feature any oxygen, for example, in organics or CH_4 (which accounts for 45% of the carbon abundance in our nominal model). We present a chemical model in Appendix B, where we decrease the CO abundance to 0.25 of the C/H and, instead, include an organic component consisting of pure carbon grains with evaporation temperature of 500 K (Semenov et al. 2003), but leaving the other parts as in our nominal model (Table 1). We find that the water ice content at [Fe/H] = 0.4 can increase to 15% for solid planetary building blocks formed exterior to the water ice line. However, this is still a factor of 3–4 smaller than the water ice content at [Fe/H] = −0.4, reproducing the trend shown in Fig. 10 from our nominal model. As the water ice content of planets formed exterior to the water ice line is crucial for planet formation, planetary composition, and even habitability, future studies of planet formation around stars with a different metallicity should take even more detailed chemical models into account. However, some models (e.g. Eistrup et al. 2018) seem to indicate that carbon is most abundant in the form of CO or CO_2, rather than organic material without any oxygen, indicating a trend more consistent with our nominal chemical model (Fig. 10).

5.5. Future observations

In the near future, GALAH will publish its third data release. This release will contain more data collected after the DR2, along with a re-analysis of the previous stars. This will include abundances of new elements (some neutron-capture elements not treated in DR2) and might incorporate new non-LTE corrections coming from 3D models, which could influence the conclusions drawn here.

In addition, over the next few years, other big spectroscopic surveys will start their operations. In particular, 4MOST (4m Multi-Object Spectroscopic Telescope; more information on all the surveys can be found in de Jong et al. 2019) will start observations at the end of 2021 from the VISTA telescope in Chile, with a plan to observe almost 10 million stars in the Milky Way. Related to this star-planet connection, more than 2.5 million objects will be observed in the Galactic disc, both in high ($R \sim 20\,000$) and low resolution ($R \sim 5000$). In particular, for the high resolution disc and bulge survey, at least 15% of the targets will be observed also by TESS. For the high-resolution observations, more than 20 elemental abundances can be potentially derived and among this list, all the elements that are included in this work are going to be observed, including sulfur. The potential results that may come of 4MOST is incredible: the massive sample homogeneously analysed with the big overlap with the planet transit mission TESS and other surveys will give an enormous amount of constraints and data for planet formation theory; particularly with respect to the star-planet connection.

6. Summary

In this study we combined observations of elemental abundances of stars (Fig. 1) to the composition of planet-forming material and planet formation. Our model is based on the assumption that the host star abundance is directly linked to the abundances of elements within the planet-forming protoplanetary disc. To calculate the exact composition of solid planetary building blocks interior and exterior to the water ice line we have used a simple equilibrium chemical model (Table 1) and show variations of that model in Appendix B.

Our model predicts that the elemental composition of planetary building blocks formed completely interior to the water ice line ($T > 150$ K) and that it is very similar across all host star metallicities (Fig. 11). However, the elemental mass fractions of planetary building blocks forming completely exterior to the water ice line ($T < 150$ K) are very different depending on the host star metallicity. In particular, the water ice mass fraction is reduced from close to 50% at [Fe/H] = −0.4 to only ∼6% at [Fe/H] = 0.4 (Fig. 10) within our chemical model. This has important consequences for the formation, composition, and habitability of planets.

Planet formation models (Sect. 4 and Appendix C) show that the water ice content of the formed planets can be mixed between the extreme states of zero water ice and the maximal content allowed for the specific disc composition due to planetary migration and the evolution of the water ice line (see also Bitsch et al. 2019b). This trend has also been found in other planet formation simulations just using solar composition (e.g. Alessi et al. 2017).

Additionally, a change in the water ice fraction alters the formation pathway of planets (Bitsch & Johansen 2016). In particular, Bitsch & Johansen (2016) show that discs with similar metallicity but a higher water ice fraction form more giant planets. The simulations we present here show that the water ice fraction around high metallicity stars is very low and, thus, the condensation of water ice molecules to assist grains growth (Ros et al. 2019) might not be the main cause for triggering giant planet formation. Instead, planetesimal formation might be triggered by the overall large metallicity (Yang et al. 2017). The effects of water ice condensation for grain growth might, thus, be more important for stars with [Fe/H] < 0.2, while its effect might be very small around stars with an even higher metallicity. Hence, we speculate that giant planet formation around stars with [Fe/H] < 0.2 might be triggered at the water ice line, but it could be triggered instead at the CO ice line for stars with an even higher metallicity due to the large CO abundance caused by the high C/O ratio (Fig. 12) which, in turn, could cause grain growth at the CO line due to CO condensation.

The change of the water ice fraction with host star metallicity also directly impacts the habitability of planets formed in these systems. Systems with intrinsically lower or no water abundance might not be able to form planets with enough water for them to be habitable. Future characterization of atmospheres of exoplanets in the habitable zone should, thus, take the host star abundances into account.

Our study clearly indicates a large impact on the planetary composition and planet formation pathway depending on the chemical composition of the host star. We encourage future studies of planet formation that strive to span a wide range of host star metallicities that would include the effects of different abundances of different elements.

Acknowledgements. B.B. thanks the European Research Council (ERC Starting Grant 757 448-PAMDORA) for their financial support. C.B.'s work was supported by Sonderforschungsbereich SFB 881 "The Milky Way System" (subproject A9) of the German Research Foundation (DFG). We thank the referee for her/his comments.

References

Abbot, D. S., Cowan, N. B., & Ciesla, F. J. 2012, ApJ, 756, 178
Adams, E. R., Seager, S., & Elkins-Tanton, L. 2008, ApJ, 673, 1160
Adibekyan, V. Z., Sousa, S. G., Santos, N. C., et al. 2012, A&A, 545, A32
Alessi, M., Pudritz, R. E., & Cridland, A. J. 2017, MNRAS, 464, 428
Ali-Dib, M. 2017, MNRAS, 467, 2845
Amarsi, A. M., & Asplund, M. 2017, MNRAS, 464, 264
Amarsi, A. M., Asplund, M., Collet, R., & Leenaarts, J. 2016a, MNRAS, 455, 3735
Amarsi, A. M., Lind, K., Asplund, M., Barklem, P. S., & Collet, R. 2016b, MNRAS, 463, 1518
Amarsi, A. M., Nissen, P. E., Asplund, M., Lind, K., & Barklem, P. S. 2019, A&A, 622, L4
Asplund, M., Grevesse, N., Sauval, A. J., & Scott, P. 2009, ARA&A, 47, pp. 481
Ataiee, S., Baruteau, C., Alibert, Y., & Benz, W. 2018, A&A, 615, A110
Baillié, K., Charnoz, S., & Pantin, E. 2015, A&A, 577, A65
Baruteau, C., Crida, A., Paardekooper, S. J., et al. 2014, Protostars and Planets VI, eds. H Beuther, R. S. Klessen, C. P. Dullemond, & T. Henning (Tucson, AZ: University of Arizona Press), 914, 667
Battistini, C., & Bensby, T. 2015, A&A, 577, A9
Battistini, C., & Bensby, T. 2016, A&A, 586, A49
Bensby, T., Feltzing, S., & Oey, M. S. 2014, A&A, 562, A71
Bensby, T., Feltzing, S., Gould, A., et al. 2017, A&A, 605, A89
Benz, W., Slattery, W. L., & Cameron, A. G. W. 1988, Icarus, 74, 516
Bergin, E. A., Blake, G. A., Ciesla, F., Hirschmann, M. M., & Li, J. 2015, Proc. Natl. Acad. Sci., 112, 8965
Bitsch, B., & Johansen, A. 2016, A&A, 590, A101
Bitsch, B., & Johansen, A. 2017, Astrophys. Space Sci. Lib., 445, 339
Bitsch, B., & Kley, W. 2010, A&A, 523, A30
Bitsch, B., Johansen, A., Lambrechts, M., & Morbidelli, A. 2015a, A&A, 575, A28
Bitsch, B., Lambrechts, M., & Johansen, A. 2015b, A&A, 582, A112
Bitsch, B., Forsberg, R., Liu, F., & Johansen, A. 2018a, MNRAS, 479, 3690
Bitsch, B., Morbidelli, A., Johansen, A., et al. 2018b, A&A, 612, A30
Bitsch, B., Izidoro, A., Johansen, A., et al. 2019a, A&A, 623, A88
Bitsch, B., Raymond, S. N., & Izidoro, A. 2019b, A&A, 624, A109
Bond, J. C., O'Brien, D. P., & Lauretta, D. S. 2010, ApJ, 715, 1050
Booth, R. A., Clarke, C. J., Madhusudhan, N., & Ilee, J. D. 2017, MNRAS, 469, p. 3994
Buchhave, L. A., Latham, D. W., Johansen, A., et al. 2012, Nature, 486, 375
Buchhave, L. A., Dressing, C. D., Dumusque, X., et al. 2016, AJ, 152, id. 160
Buchhave, L. A., Bitsch, B., Johansen, A., et al. 2018, ApJ, 856, 37
Buder, S., Asplund, M., Duong, L., et al. 2018, MNRAS, 478, 4513
Burbidge, E. M., Burbidge, G. R., Fowler, W. A., & Hoyle, F. 1957, Rev. Mod. Phys., 29, 547
Cabral, N., Lagarde, N., Reylé, C., Guilbert-Lepoutre, A., & Robin, A. C. 2019, A&A, 622, A49
Caffau, E., Bonifacio, P., Faraggiana, R., et al. 2005, A&A, 441, 533
Chatterjee, S., & Tan, J. C. 2014, ApJ, 780, 53
Chen, Y. Q., Nissen, P. E., Zhao, G., & Asplund, M. 2002, A&A, 390, 225
Cossou, C., Raymond, S. N., Hersant, F., & Pierens, A. 2014, A&A, 569, A56
Cridland, A. J., Eistrup, C., & van Dishoeck, E. F. 2019, A&A, 627, A127
de Jong, R. S., Agertz, O., Berbel, A. A., et al. 2019, The Messenger, 175, 3
Dorn, C., Mosegaard, K., Grimm, S. L., & Alibert, Y. 2018, ApJ, 865, 20
Dorn, C., Harrison, J. H. D., Bonsor, A., & Hands, T. O. 2019, MNRAS, 484, 712
Drążkowska, J., & Alibert, Y. 2017, A&A, 608, A92
Duffau, S., Caffau, E., Sbordone, L., et al. 2017, A&A, 604, A128
Eistrup, C., Walsh, C., & van Dishoeck, E. F. 2016, A&A, 595, A83
Eistrup, C., Walsh, C., & van Dishoeck, E. F. 2018, A&A, 613, A14
Fischer, D. A., & Valenti, J. 2005, ApJ, 622, 1102
Fortney, J. J., Marley, M. S., & Barnes, J. W. 2007, ApJ, 659, 1661
Fulton, B. J., Petigura, E. A., Howard, A. W., et al. 2017, AJ, 154, 109
Furuya, K., Aikawa, Y., Hincelin, U., et al. 2015, A&A, 584, A124
Gillon, M., Jehin, E., Lederer, S. M., et al. 2016, Nature, 533, 221
Gillon, M., Triaud, A. H. M. J., Demory, B.-O., et al. 2017, Nature, 542, 456
Guenther, E. W., Barragán, O., Dai, F., et al. 2017, A&A, 608, A93
Gupta, A., & Schlichting, H. E. 2019, MNRAS, 487, 24
Hansen, B. M. S., & Murray, N. 2012, ApJ, 751, 158
Henning, T., & Semenov, D. 2013, Chem. Rev. 113, 9016
Hinkel, N. R., & Unterborn, C. T. 2018, ApJ, 853, 83
Ida, S., & Guillot, T. 2016, A&A, 596, L3
Ida, S., & Lin, D. N. C. 2004, ApJ, 604, pp. 388
Ida, S., & Lin, D. N. C. 2008, ApJ, 685, 584
Ida, S., & Lin, D. N. C. 2010, ApJ, 719, 810
Izidoro, A., Ogihara, M., Raymond, S. N., et al. 2017, MNRAS, 470, 1750
Izidoro, A., Bitsch, B., Raymond, S. N., et al. 2019, A&A, submitted [arXiv:1902.08772]
Jin, S., & Mordasini, C. 2018, ApJ, 853, 163
Johansen, A., & Lacerda, P. 2010, MNRAS, 404, 475
Johansen, A., & Lambrechts, M. 2017, AREP, 45
Johansen, A., Blum, J., Tanaka, H., et al. 2014, Protostars and Protoplanets VI (Tucson, AZ: University of Arizona Press), 547
Johnson, J. A., Aller, K. M., Howard, A. W., & Crepp, J. R. 2010, PASP, 122, 905
Jönsson, H., Ryde, N., Nissen, P. E., et al. 2011, A&A, 530, A144
Kobayashi, C., & Nakasato, N. 2011, ApJ, 729, 16
Kobayashi, C., Umeda, H., Nomoto, K., Tominaga, N., & Ohkubo, T. 2006, ApJ, 653, 1145
Lambrechts, M., & Johansen, A. 2012, A&A, 544, A32
Lambrechts, M., Johansen, A., & Morbidelli, A. 2014, A&A, 572, A35
Lambrechts, M., Morbidelli, A., Jacobson, S. A., et al. 2019, A&A, 627, A83
Lee, E. J., & Chiang, E. 2016, ApJ, 817, 90
Ligi, R., Dorn, C., Crida, A., et al. 2019, A&A, 631, A92
Lodders, K. 2003, ApJ, 591, 1220
Lopez, E. D., & Fortney, J. J. 2014, ApJ, 792, 1
Madhusudhan, N., Crouzet, N., McCullough, P. R., Deming, D., & Hedges, C. 2014, ApJ, 791, L9
Madhusudhan, N., Bitsch, B., Johansen, A., & Eriksson, L. 2017, MNRAS, 469, 4102
Marboeuf, U., Thiabaud, A., Alibert, Y., Cabral, N., & Benz, W. 2014, A&A, 570, A36
Matteucci, F., & Greggio, L. 1986, A&A, 154, 279
Matteucci, F., Spitoni, E., Recchi, S., & Valiante, R. 2009, A&A, 501, 531
Mayor, M., Marmier, M., Lovis, C., et al. 2011, ArXiv e-prints [arXiv:1109.2497]

McDonough, W., & Sun, S. 1995, Chem. Geol., 120, 223
McNeil, D. S., & Nelson, R. P. 2010, MNRAS, 401, 1691
Morbidelli, A., Bitsch, B., Crida, A., et al. 2016, Icarus, 267, 368
Mordasini, C., Alibert, Y., & Benz, W. 2009, A&A, 501, 1139
Mulders, G. D., Pascucci, I., Apai, D., & Ciesla, F. J. 2018, AJ, 156, 24
Ndugu, N., Bitsch, B., & Jurua, E. 2018, MNRAS, 474, 886
Ness, M., Hogg, D. W., Rix, H. W., Ho, A. Y. Q., & Zasowski, G. 2015, ApJ, 808, 16
Öberg, K. I., Murray-Clay, R. A., & Bergin, E. 2011, ApJ, 743, L16
Ogihara, M., & Ida, S. 2009, ApJ, 699, 824
Ogihara, M., Morbidelli, A., & Guillot, T. 2015, A&A, 578, A36
Ogihara, M., Kokubo, E., Suzuki, T. K., & Morbidelli, A. 2018, A&A, 615, A63
Oka, A., Nakamoto, T., & Ida, S. 2011, ApJ, 738, 141
Ormel, C. W., & Klahr, H. H. 2010, A&A, 520, A43
Osorio, Y., Barklem, P. S., Lind, K., et al. 2015, A&A, 579, A53
Owen, J. E., & Wu, Y. 2013, ApJ, 775, 105
Owen, J. E., & Wu, Y. 2017, ApJ, 847, 29
Paardekooper, S.-J., & Mellema, G. 2006, A&A, 453, 1129
Paardekooper, S. J., Baruteau, C., & Kley, W. 2011, MNRAS, 410, 293
Piskunov, N., & Valenti, J. A. 2017, A&A, 597, A16
Putirka, K. D., & Rarick, J. C. 2019, Am. Mineral., 104, 817
Raymond, S. N., & Izidoro, A. 2017, Icarus, 297, 134
Raymond, S. N., O'Brien, D. P., Morbidelli, A., & Kaib, N. A. 2009, Icarus, 203, 644
Raymond, S. N., Boulet, T., Izidoro, A., Esteves, L., & Bitsch, B. 2018, MNRAS, 479, L81
Ronco, M. P., Thiabaud, A., Marboeuf, U., et al. 2015, Boletin de la Asociacion Argentina de Astronomia La Plata Argentina, 57, 251
Ros, K., & Johansen, A. 2013, A&A, 552, A137
Ros, K., Johansen, A., Riipinen, I., & Schlesinger, D. 2019, A&A, 629, A65
Santos, N. C., Israelia, G., & Mayor, M. 2004, A&A, 415, 1153
Santos, N. C., Adibekyan, V., Mordasini, C., et al. 2015, A&A, 580, L13
Santos, N. C., Adibekyan, V., Dorn, C., et al. 2017, A&A, 608, A94
Schoonenberg, D., & Ormel, C. W. 2017, A&A, 602, A21
Schoonenberg, D., Liu, B., Ormel, C. W., & Dorn, C. 2019, A&A, 627, A149
Seager, S. 2013, Science, 340, 577
Seager, S., Kuchner, M., Hier-Majumder, C. A., & Militzer, B. 2007, ApJ, 669, 1279
Selsis, F., Chazelas, B., Bordé, P., et al. 2007, Icarus, 191, 453
Semenov, D., Henning, T., Helling, C., Ilgner, M., & Sedlmayr, E. 2003, A&A, 410, 611
Smiljanic, R., Korn, A. J., Bergemann, M., et al. 2014, A&A, 570, A122
Sotin, C., Grasset, O., & Mocquet, A. 2007, Icarus, 191, 337
Sousa, S. G., Adibekyan, V., Santos, N. C., et al. 2019, MNRAS, 485, 3981
Stammler, S. M., Birnstiel, T., Panić, O., Dullemond, C. P., & Dominik, C. 2017, A&A, 600, A140
Takeda, Y., Omiya, M., Harakawa, H., & Sato, B. 2016, PASJ, 68, 81
Terquem, C., & Papaloizou, J. C. B. 2007, ApJ, 654, 1110
Thiabaud, A., Marbouf, U., Alibert, Y., Leya, I., & Mezger, K. 2015, A&A, 574, A138
Thielemann, F. K., Argast, D., Brachwitz, F., et al. 2002, Ap&SS, 281, 25
Turbo-King, M., Tang, B. R., Habeertable, Z., et al. 2017, JoA, submitted [arXiv:1703.10803]
Unterborn, C. T., & Panero, W. R. 2017, ApJ, 845, 61
Valencia, D., Sasselov, D. D., & O'Connell, R. J. 2007, ApJ, 665, 1413
Valenti, J. A., & Piskunov, N. 1996, A&AS, 118, 595
Valiante, R., Matteucci, F., Recchi, S., & Calura, F. 2009, New A, 14, 638
Van Eylen, V., Agentoft, C., Lundkvist, M. S., et al. 2018, MNRAS, 479, 4786
Vazan, A., Ormel, C. W., & Dominik, C. 2018, A&A, 610, L1
Weiss, L. M., Marcy, G. W., Petigura, E. A., et al. 2018, AJ, 155, 48
Yang, C.-C., Johansen, A., & Carrera, D. 2017, A&A, 606, A80
Zeng, L., & Sasselov, D. 2013, PASP, 125, 227
Zeng, L., Jacobsen, S. B., Sasselov, D. D., et al. 2019, PNAS, 116, 9723
Zhu, W. 2019, AAS, submitted [arXiv:1907.02074]
Zhu, W., & Wu, Y. 2018, AJ, 156, 92

Appendix A: Stellar abundances

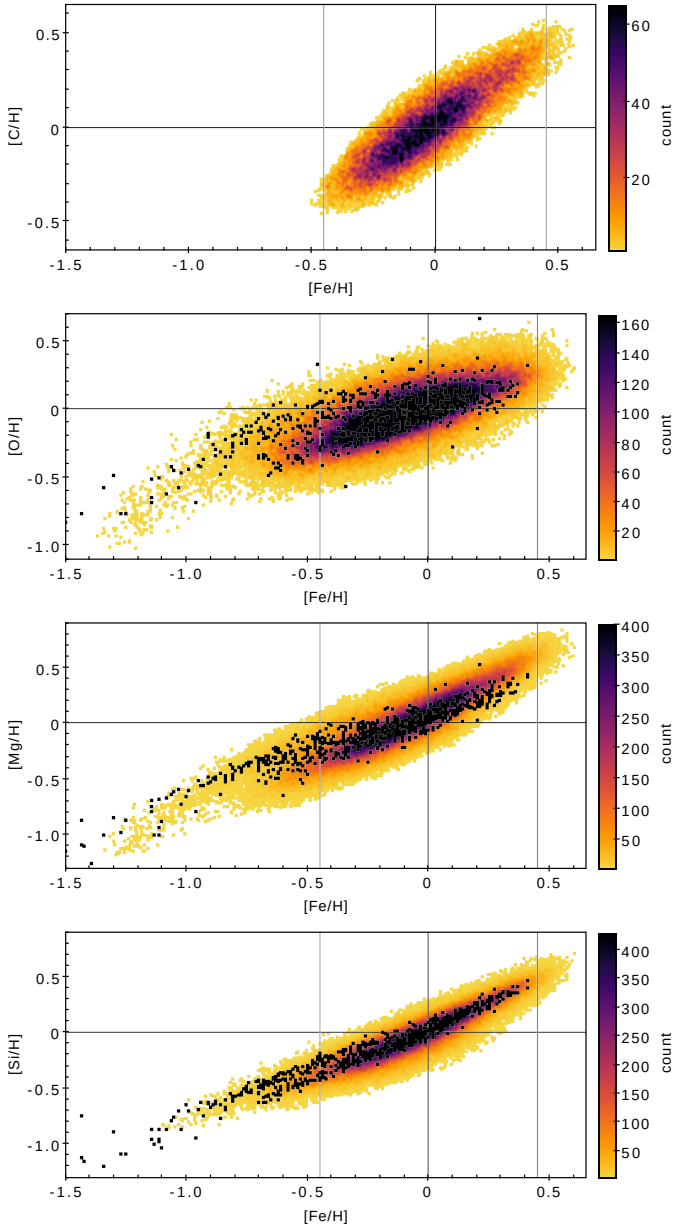

Fig. A.1. Carbon, oxygen, magnesium, and silicon abundances for the stars in the GALAH sample (Buder et al. 2018). Black dots mark the data from the detailed survey of Bensby et al. (2014), which does not include carbon. This plot illustrates that the trends of the GALAH survey agree with previous studies and that there is some variations within the sample. The black vertical lines at [Fe/H] = −0.45 and 0.45 indicate the [Fe/H] span used in Fig. 1, while the lines at [Fe/H] = 0 and [X/H] = 0 mark the solar value.

We show in Fig. A.1 the stellar abundances of carbon, oxygen, magnesium, and silicon for the GALAH sample of stars used in our work. The overall trends agree with the previous study of Bensby et al. (2014) and the values used for our calculations are shown in Table A.1 and plotted in Fig. 1.

Appendix B: Carbon contribution

The carbon fraction of minor bodies in the Solar System is much higher than the carbon content within the Earth (e.g. Bergin et al. 2015), implying that the history of the chemical composition could change with orbital distance and planet formation models have to account for these effects. In our model, the water ice abundance is governed by the amount of free oxygen that does not contribute to rock-forming materials or CO and CO_2 – and not by orbital distance. Thus, an elevated C/O ratio (Fig. 12) reduces the amount of free oxygen that can form water ice. As a consequence, the amount of carbon that forms carbon chain molecules without oxygen can influence the water ice content in our model.

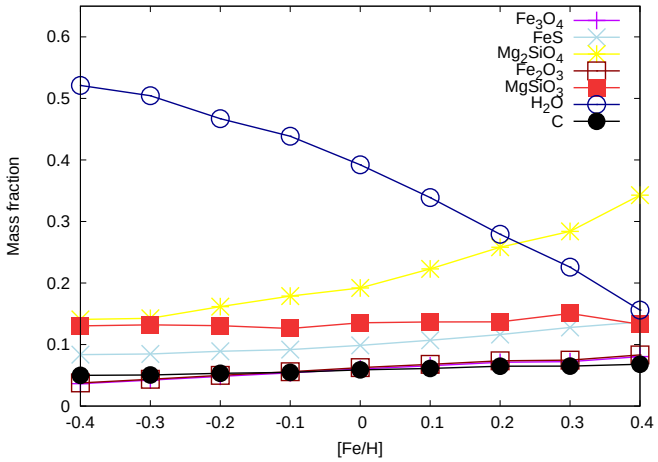

Fig. B.1. Solid mass fractions of solid planetary building blocks formed exterior to the water ice line as function of [Fe/H] where 20% of the C/H is assumed to be in carbon chains with an evaporation temperature of 500 K and only 25% of the C/H is assumed to be bound in CO. The trend for H_2O is similar to Fig. 10. However, the water ice abundance at large [Fe/H] is about a factor of 2–3 larger, while it stays roughly constant for low [Fe/H] compared to the nominal chemical model (Fig. 10).

In our nominal model (Table 1) we included a fraction of 45% of the C/H in organics (methane). We relax this approach here for testing purposes and reduce the CO content to 25%, and we also include a 20% C/H fraction in pure carbon grains with an evaporation temperature of 500 K (e.g. Semenov et al. 2003), bringing the total carbon content that forms non-oxygen-bearing molecules to 65% of the whole C/H, thus increasing the water content. We show these trends in Fig. B.1.

Even with these assumptions, the general trend shown in Fig. 10 holds and the water ice content decreases by nearly a factor of 3 from [Fe/H] = −0.4 to [Fe/H] = 0.4. The difference to our nominal chemical model is larger for super-solar [Fe/H] compared to sub-solar [Fe/H]. This is caused by the low C/O ratio at low [Fe/H] (Fig. 12), so that the effect of forming less CO compared to the total amount of oxygen that can form water is not significant. For high [Fe/H], the C/O ratio is much larger, resulting that the effect of forming less CO can actually increase the amount of oxygen that can from water. On the other hand, at high [Fe/H] also the rock-forming species that bind oxygen like Fe, Si, and Mg are more abundant than oxygen implying that the water ice ratio will decrease with increasing [Fe/H] independently of how much oxygen is bound in carbon to form CO or CO_2. The exact water content though can be estimated more accurately with more detailed chemical models, however, detailed models seem to indicate that the ratio between CO to CO_2 to non-oxygen bearing carbon molecules is maximally equal, where in most cases the non-oxygen bearing carbon molecules are less abundant than CO and CO_2 (Eistrup et al. 2018), which points to a water ice ratio as predicted by our nominal model (Fig. 10).

Table A.1. Stellar abundances as derived from the GALAH catalogue (Buder et al. 2018).

[Fe/H]	σ[Fe/H]	[Si/H]	σ[Si/H]	[Mg/H]	σ[Mg/H]	[C/H]	σ[C/H]	[O/H]	σ[O/H]
−0.4	0.02	−0.32	0.06	−0.26	0.08	−0.29	0.05	−0.19	0.08
−0.3	0.02	−0.25	0.06	−0.19	0.07	−0.22	0.06	−0.13	0.08
−0.2	0.02	−0.17	0.06	−0.10	0.07	−0.14	0.06	−0.08	0.08
−0.1	0.02	−0.09	0.06	−0.01	0.07	−0.06	0.07	−0.02	0.07
0.0	0.03	0.00	0.06	0.08	0.07	0.03	0.07	0.03	0.07
0.1	0.02	0.10	0.06	0.19	0.07	0.11	0.07	0.08	0.07
0.2	0.02	0.20	0.06	0.30	0.07	0.20	0.07	0.13	0.07
0.3	0.02	0.32	0.05	0.42	0.06	0.28	0.06	0.19	0.07
0.4	0.03	0.41	0.05	0.53	0.06	0.36	0.06	0.23	0.07

Notes. This data is used to plot Fig. 1.

Appendix C: Planet formation

For our planet formation model, we follow the core accretion scenario where planetary cores grow by pebble accretion (Ormel & Klahr 2010; Johansen & Lacerda 2010; Lambrechts & Johansen 2012) and migrate through type-I migration using the prescription of Paardekooper et al. (2011). We use the disc model outlined in Bitsch et al. (2015a), where we either let the disc evolve in time or not to illustrate its influence on planetary composition similar to the principles outlined in Bitsch et al. (2019b). In addition, we adopt two different α parameters for planetary migration to illustrate the effects of inward or outward migration close to the water ice line on the planetary composition as in Bitsch et al. (2019b).

The details of our pebble accretion model are described in Bitsch et al. (2015b) and here we just repeat the main points. We use a fixed pebble Stokesnumber $\tau_\mathrm{f} = 0.1$ through the whole disc. The radial drift speed of the pebbles is given by

$$v_\mathrm{r,peb} = 2\frac{\tau_\mathrm{f}}{\tau_\mathrm{f}+1}\eta v_\mathrm{K}, \tag{C.1}$$

where η is the radial pressure gradient at the pebbles position and v_K is the Keplerian speed of the gas. We use a pebble flux of

$$\dot{M}_\mathrm{peb} = 2\times10^{-4}\times10^{[\mathrm{Fe/H}]}\exp(-t/10^6\,\mathrm{yr})\frac{\mathrm{M_E}}{\mathrm{yr}}, \tag{C.2}$$

where the component $10^{[\mathrm{Fe/H}]}$ describes a scaling with the host star metallicity. In addition, we use an exponential decrease of the pebble flux in time t. With this pebble flux we can calculate the pebble surface density at the location of the planet r_p in the following way

$$\Sigma_\mathrm{peb} = \frac{\dot{M}_\mathrm{peb}}{2\pi r_\mathrm{p} v_\mathrm{r}}. \tag{C.3}$$

The 2D Hill accretion rate onto the planetary core is then given as

$$\dot{M}_\mathrm{core} = 2 r_\mathrm{H} v_\mathrm{H} \Sigma_\mathrm{peb}, \tag{C.4}$$

with r_H being the planetary Hill radius and $v_\mathrm{H} = \Omega_\mathrm{K} r_\mathrm{H}$ being the Hill speed. The planetary growth is stopped at the pebble isolation mass (Lambrechts et al. 2014; Bitsch et al. 2018b; Ataiee et al. 2018), when the planet starts to carve a small gap in the protoplanetary disc which exerts a pressure bump exterior to it, stopping the inward flux of pebbles (Paardekooper & Mellema 2006) and thus pebble accretion. The slightly simplified pebble isolation mass (Bitsch et al. 2018b) is given as

$$M_\mathrm{iso} = 25\left(\frac{H/r}{0.05}\right)^3 M_\mathrm{E}. \tag{C.5}$$

As soon as the planet reaches its pebble isolation mass, we stop pebble accretion, but at the same time we do not model the gas accretion component because we are only interested in the composition of the planetary core.

The migration of the planet is determined by the formula of Paardekooper et al. (2011). In this formula, the migration direction and speed depends crucially on the radial gradients of gas surface density, along with temperature and entropy. In addition, outward migration by the entropy-driven corotation torque can only happen if the viscosity is large enough. In the disc model of Bitsch et al. (2015a) this leads to a region of outward migration attached to the water ice line, if $\alpha_\mathrm{mig} > 0.001$, where the nominal value in this model is $\alpha_\mathrm{mig} = 0.0054$. We also test a variation with $\alpha_\mathrm{mig} = 0.0001$ which results in only inward migration at the water ice line, changing the water content to smaller values because the assembly of the planets can be completed interior to the water ice line (Bitsch et al. 2019b). In Sect. 4 we use $\alpha_\mathrm{mig} = 0.0054$, meaning that planets can migrate inwards and outwards. Here we show the results of different migration prescriptions and their influence on the water ice content of planets in a similar fashion as in Bitsch et al. (2019b).

We place planetary embryos of initially 0.01 Earth masses at different initial positions r_0 in discs that are initially already 0.5 Myr old (in order to account for the formation of the planetary embryo). We then vary the [Fe/H] of the host star and calculate the water ice fraction of the formed planets via our nominal chemical model. In Fig. C.1 we show the water ice content of formed planets in our model for three different assumptions: (i) a non-evolving disc with only inward planetary migration modelled with $\alpha_\mathrm{mig} = 0.0001$ (top); (ii) an evolving disc with only inward planetary migration (middle); and (iii) an evolving discs where planets can migrate inwards and/or outwards with $\alpha_\mathrm{mig} = 0.0054$ (bottom). The final planetary masses are between 3 and 10 Earth masses in all models and if planetary migration is only inwards, planets reach the inner edge at 0.1 AU, while in the scenario with outward migration, planets are trapped at around 1.8 AU, which corresponds to the outer edge of the region of outward migration in that disc model (Bitsch et al. 2015a).

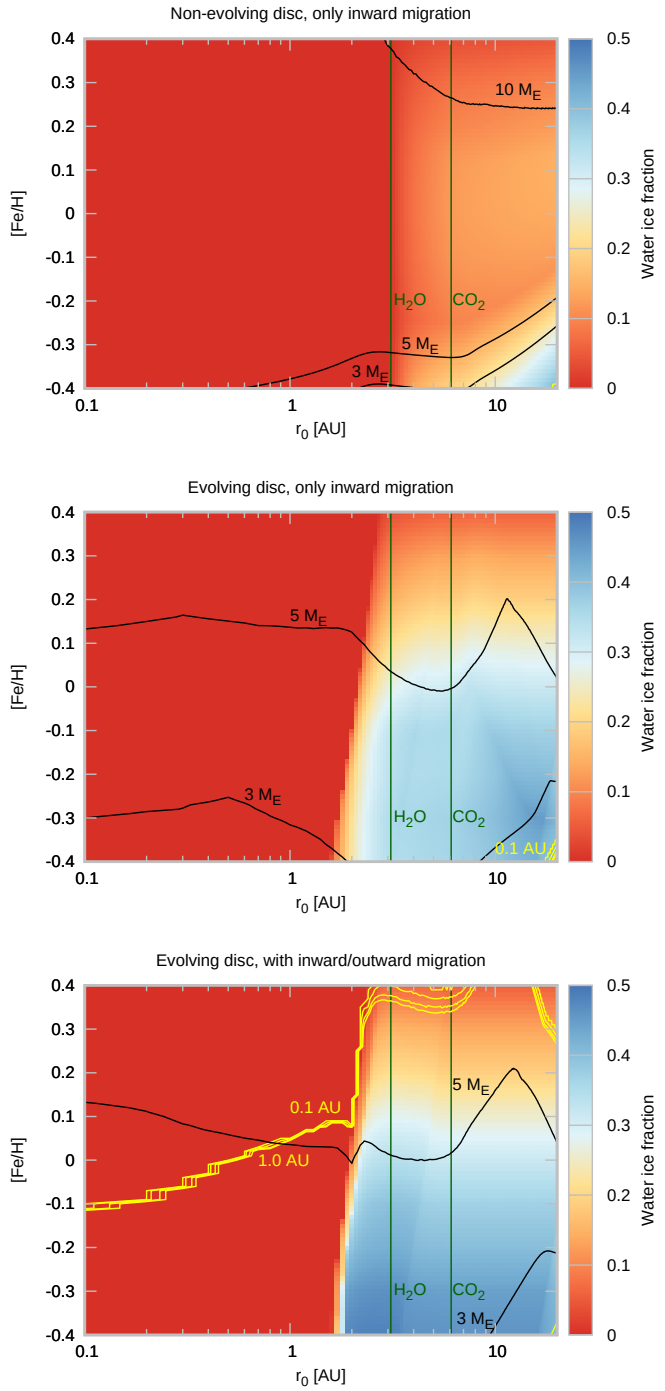

Fig. C.1. Final water ice content of planets formed with initial position r_0 and around stars with metallicity of [Fe/H] in either non-involving discs with only inward migration (*top*), evolving discs with only inward migration (*middle*), and evolving discs with inward and outward migration (*bottom*). Planets are injected at $t_0 = 0.5$ Myr. The black and yellow lines respectively mark the final orbital position (0.1, 0.3, 0.5 and 1.0 AU) and masses of the planets. In the simulations presented in the top two panels, nearly all planets migrate to the inner edge at 0.1 AU. Green vertical lines depict the H_2O and CO_2 ice lines at the beginning of the simulations. H_2O and CO_2 are in icy form exterior to these ice lines. Due to the disc's evolution in time (*middle and bottom*), the water ice line moves inwards, so that the water ice line can sweep over slow growing planets initially interior to the water ice line allowing them to have a water ice contribution.

For the non-evolving disc with only inward migration, the results are as expected. Planets starting to form exterior to the water ice line initially accrete water ice and then migrate into the inner disc where they complete their assembly and thus feature a low water ice content. All planets in this case reach 0.1 AU. Planets forming exterior to the CO_2 ice line feature a higher water ice content, because they can finish most of their growth exterior to the water ice line and thus accrete water ice. This is also reflected by the water ice gradient of the planets with increasing initial planetary position, meaning that the farther the planetary embryo is placed exterior to the water ice line, the higher its water ice content. This result is consistent with Bitsch et al. (2019b) derived for solar metallicity. In addition with increasing [Fe/H] the water ice content decreases, as shown in the main paper.

In case the disc evolves, the water ice line moves inward in time due to the decrease in viscous heating and even planetary embryos that are initially placed interior to the water ice line can accrete water ice because the evolution of the water ice line is initially faster than planet migration (Bitsch et al. 2019b). If planetary accretion is faster, planets grow quicker and they can migrate inwards faster, avoiding the sweep of the inward moving water ice line. This is for example the case at high [Fe/H], where the pebble flux is larger and thus accretion is faster and only planets initially slightly interior to the water ice line can accrete some water ice. The planets in this scenario all migrate to the inner edge of the disc at 0.1 AU.

In the case of an evolving disc where planets can migrate inward and outwards, the water ice content of the fully grown planets is highest of these three models. This is caused by the fact that planets in this model migrate outwards exterior to the water ice line where they then complete their assembly and, thus, accrete all their mass with a water ice component (Bitsch et al. 2019b). In the end, planets either migrate to the inner edge of the disc at 0.1 AU or stay trapped in the region of outward migration exterior to 1 AU until disc dissipation. The water ice component of the planets decreases slightly for planetary seeds forming exterior to a few AU because the disc becomes so cold that the planets also accrete a fraction of CO_2 ice. This decreases the relative water ice component of the accreted material and results in a lower water ice fraction of the formed planets.

In any case, all of these simulations clearly show that the water ice content of the formed planets is a mixture and it is always in between the states of zero water ice (planets formed completely interior to the water ice line) and up to the maximal water ice content allowed in the chemical model (planets that form completely exterior to the water ice line). The planet formation simulations also clearly demonstrate the water ice gradient from low [Fe/H] to high [Fe/H], as outlined in the main part of the paper and Sect. 4.